A staggered discontinuous Galerkin method for the simulation of seismic waves with surface topography

Eric T. Chung*; Chi Yeung Lam*; Jianliang Qian†

**Department of Mathematics*

The Chinese University of Hong Kong, Hong Kong SAR. Email: tschung@math.cuhk.edu.hk, cylam@math.cuhk.edu.hk

†*Department of Mathematics, Michigan State University, East Lansing, MI 48824. Email: qian@math.msu.edu*

(March 18, 2015)

Running head: **SDG method for seismic waves**

ABSTRACT

Accurate simulation of seismic waves is of critical importance in a variety of geophysical applications. Based on recent works on staggered discontinuous Galerkin methods, we propose for the simulations of seismic waves a new method which has energy conservation and extremely low grid dispersion, so that it naturally provides accurate numerical simulations of wave propagation useful for geophysical applications and is a generalization of classical staggered grid finite difference methods. Moreover, it can handle with ease irregular surface topography and discontinuities in the subsurface models. Our new method discretizes the velocity and the stress tensor on this staggered grid, with continuity imposed on different parts of the mesh. The symmetry of the stress tensor is enforced by the Lagrange multiplier technique. The resulting method is an explicit scheme,

requiring the solutions of a block diagonal system and a local saddle point system in each time step, and is therefore very efficient. In order to tailor our scheme to Rayleigh waves, we develop a mortar formulation of our method. In particular, a fine mesh is used near the free surface and a coarse mesh is used in the rest of the domain. The two meshes are in general not matching, and the continuity of the velocity at the interface is enforced by a Lagrange multiplier. The resulting method is also efficient in time marching. We also give a stability analysis of the scheme and an explicit bound for the time step size. In addition, we present some numerical results to show that our method is able to preserve the wave energy and accurately compute the Rayleigh waves. Moreover, the mortar formulation gives a significant speed up compared with the use of a uniform fine mesh, and provides an efficient tool for the simulation of Rayleigh waves.

INTRODUCTION

Accurate simulation of seismic and Rayleigh waves is of critical importance in a variety of geophysical applications, such as exploration geophysics, geotechnical characterization, and earthquake-related damage assessment (Aki and Richards, 2002). Consequently, it is a long-studied topic in geophysics in that many challenging problems arise in designing for Rayleigh wave simulation an accurate method which ideally should enjoy low grid dispersion, provide accurate long-time/long-range wave propagation, and allow irregular surface topography and discontinuities in the subsurface model. Based on recent works in Chung and Engquist (2006, 2009), we design a staggered discontinuous Galerkin method to tackle exactly these challenges: the new method has extremely low grid dispersion as shown in Chung et al. (2013a) and Chan et al. (2013); it has the energy-conservation property (Chung and Engquist, 2006, 2009) so that it naturally provides accurate numerical simulations of wave propagation useful for geophysical applications and is a generalization of classical staggered grid finite difference methods. Moreover, it can handle with ease irregular surface topography and discontinuities in the subsurface models, since our method is based on a novel triangular staggered mesh.

In the literature, simulations of Rayleigh waves have been mainly tackled with finite-difference methods (FDM) and finite-element methods (FEM). In terms of FDM for Rayleigh waves, most of these methods are based on staggered-grid FDMs proposed by Madariaga (1976), Virieux (1986) and Levander (1988). When the surface topography is flat, the free-surface boundary condition associated with Rayleigh waves is relatively easy to handle in a staggered-grid FDM. In Bohlen and Saenger (2006), the staggered-grid and the rotated staggered-grid FDMs are applied to simulate

Rayleigh waves with flat surface topography, and accuracy for both methods is carefully studied. It is well-known that one needs more points per wavelength for surface waves than body waves since the surface wave in the case of flat topography mainly travels horizontally and decays exponentially in the vertical direction. Therefore, one needs to use more points in the vertical direction in order to capture the sharp decay. To overcome this increase in the number of unknowns near the surface, Kosloff and Carcione (2010) proposes a variable-grid-spacing method in which the spatial grid is finer near the surface and coarser far away from the surface and the staggered sine and cosine transforms are applied to compute spatial derivatives; the resulting method is highly accurate and is able to handle propagation of Rayleigh waves at large offsets.

When the surface topography is non-flat, two remedies are proposed to treat free-surface boundary conditions in the setting of a staggered-grid FDM: one option is to use a staircase approximation to the non-flat free surface topography, another option is to match the free surface topography by deforming computational grids. When applying staircase approximation to the non-flat free surface topography, Levander (1988) originally proposed the stress-image technique to update the veolocities for grid nodes on (flat) free surfaces, and Robertsson (1996) proposed an extension of this method, in which the grid nodes are classified into seven categories with different update rules. The vacuum formulation (Zahradnik et al., 1993) is developed along the same line by setting parameters to zero above the free surface so that surface topography can be implemented in the same manner as an internal material interface. However, numerical tests have shown that the simple vacuum formulation becomes unstable when using fourth-order or higher order spatial difference operators (Graves, 1996); consequently, Zeng et al. (2012) proposed an improved vacuum formulation to incorporate surface topography, in which the parameters at the surface grid nodes are

averaged using the same scheme as for the interior grid nodes; this method is shown to be stable using fourth-order spatial difference operators without notable numerical dispersion. On the other hand, various methods are proposed to deform computational grids to match the free surface topography by using curvilinear coordinates: Hestholm and Ruud (2002); Zhang and Chen (2006); Lombard et al. (2008) in the setting of a staggered-grid FDM and Appelö and Petersson (2009) in the setting of a non-staggered-grid FDM. Since these methods involve computation of spatial derivatives in the curved grid and application of the chain rule to calculate the required cartesian spatial derivatives, Komatitsch et al. (1996) proposed a method to solve the equation directly on curved grids.

Despite the efficiency of FDMs on structured grids, implementing free-surface conditions in FDMs can be difficult on an irregular domain. Therefore, Moczo et al. (1997) presented a hybrid method in which low-order FEMs were used near boundaries while second-order FDMs were used for the rest of the model, and Ma et al. (2004) presented another hybrid method which combined low-order FEMs with a fourth-order velocity-stress staggered-grid FDM. There are certainly plenty of advantages in using FEMs for surface topography since they allow the use of triangular meshes suitable for irregular surfaces. In terms of new developments in FEM for seismic wave modeling, several different methods are popular in geophysical community as briefly summarized in Basabe and Sen (2009): the mixed finite-element method, the spectral-element method and the discontinuous Galerkin method. Raviart and Thomas (1977) introduced the mixed FEM that is suitable for the spatial approximation of the wave equation in the velocity-stress form, and Geveci (1988) analyzed its convergence. The advantage of using mixed formulations is that the energy is conserved both locally and globally, which is an important property described by wave equations.

However, when an explicit time discretization is applied, this method usually produces an implicit time-marching scheme because nondiagonal mass matrices may arise in the process, which make the explicit time-stepping inefficient. The mass-lumping technique, which is a way to approximate the mass matrix by a diagonal matrix, is developed to improve the efficiency (Becache et al., 2000; Cohen et al., 2001). However, mass-lumping technique for tetrahedral meshes is not available for arbitrary order of approximations. The spectral element method (SEM) is a class of high-order Galerkin FEMs and originally developed for fluid dynamics (Patera, 1984), and it has been successfully applied to acoustic and elastic wave propagations (Seriani and Priolo, 1994; Komatitsch and Vilotte, 1998; Komatitsch et al., 2008). Being a method designed for hexahedral meshes, the SEM makes the design of an optimal mesh cumbersome in contrast to the flexibility offered by tetrahedral meshes. The discontinuous Galerkin (DG) FEMs provides another class of methods which can overcome the above disadvantages. In particular, the DG FEMs are constructed based on tetrahedral meshes, and have block diagonal mass matrices due to the discontinuous nature of basis functions, allowing efficient time-marching. Discontinuous Galerkin method was first introduced for the neutron transport equation in Reed and Hill (1973) and Lesaint and Raviart (1974). Since then, the method has become very popular for the numerical solutions of partial differential equations. For a general introduction to the subject, see Cockburn et al. (2000); Riviere (2008); Arnold (1982). Regarding computational wave propagation, some discontinuous Galerkin methods have been proposed in Bernacki et al. (2006); Bourdel et al. (1991); Giraldo et al. (2002); Grote et al. (2006); Hu et al. (1999) for the acoustic wave equations and in Falk and Richter (1999); Johnson and Pitkäranta (1986) for the hyperbolic system. For seismic wave simulations, some discontinuous Galerkin methods have been proposed in De Basabe et al. (2008); Dumbser and

Kaser (2006); Rivière and Wheeler (2003). Furthermore, the dispersive and dissipative properties of discontinuous Galerkin methods are analyzed in Ainsworth et al. (2006) and Chan et al. (2013).

Recently, a new class of staggered discontinuous Galerkin methods based on staggered meshes was proposed and analyzed. In particular, the staggered DG (SDG) method has been successfully developed for many wave propagation problems (Chung and Engquist, 2006, 2009; Chung et al., 2013a; Chung and Ciarlet, 2013; Chung and Lee, 2012; Chan et al., 2013) and other applications (Chung et al., 2013b; Kim et al., 2013; Chung and Kim, 2014; Chung et al., 2014a; Kim et al., 2014; Chung et al., 2014b). The SDG method is typically applied to the first order formulation of wave equations, and starts with two sets of irregular, staggered grids, for each of the two unknown functions involved; furthermore, it designs two finite-element spaces on those two sets of staggered grids and carries out integration-by-parts to derive corresponding weak formulations; finally, it applies the standard leap-frog scheme for explicit time stepping. The SDG method has several distinctive features that are particularly attractive: first, it conserves the wave energy automatically; second, it is optimally convergent in both the L^2-norm and energy norm; third, it yields block-diagonal mass matrices so that very efficient explicit time-stepping is allowed; fourth, it is flexible in handling complex geometries so that free surface conditions on non-flat surfaces can be imposed easily; fifth, as shown in Chung et al. (2013a) and Chan et al. (2013), it yields solutions with extremely low dispersion errors in that the order of dispersion error in terms of grid-size for the SDG method is two orders higher than that of classical finite-difference methods based on non-staggered grids. Since the SDG method offers many advantages in computational wave propagation, it provides a competitive alternative for simulations of Rayleigh waves and seismic waves in general for models with irregular surface topography. It is therefore the purpose of this paper to develop a SDG

method for the elastic wave equation. We emphasize that the SDG method for the acoustic wave equation, for example Chung and Engquist (2006, 2009), cannot be directly applied to the elastic wave equation due to the symmetry of the stress tensor. In this paper, we construct a new SDG method using the Lagrange multiplier technique for the enforcement of the symmetry of the stress tensor. The resulting scheme retains all the advantages of the SDG method for acoustic wave equations discussed above. Moreover, due to the staggered continuity property of basis functions for the SDG method, the use of the Lagrange multiplier only gives a local saddle point system, instead of a global system common to other Lagrange multiplier techniques for FEMs. Hence, the time-marching can be done very efficiently.

In addition, a mortar formulation is developed to tailor our scheme to the simulation of Rayleigh waves. We split the computational domain in two parts, one of which is a thin layer near the free surface. A very fine mesh is used in the thin layer near the surface to capture the Rayleigh wave and a coarse mesh is used in the rest of the domain to speed up the simulations. The basis functions for the velocity in the two parts of the computational domain are totally decoupled and they are connected by the use of Lagrange multiplier. The resulting scheme is able to produce an equally accurate solution compared with solution obtained by a uniform fine mesh.

The paper is organized as follows. The paper starts with the basic formulation of the SDG method, followed by a stability analysis for the time step size. A set of numerical results are then given to show the performance of the scheme. In addition, a numerical study of dispersion error is presented. Finally, a mortar formulation is developed to tailor the scheme to Rayleigh waves. The paper ends with a conclusion.

PROBLEM SETTING

The simulation of Rayleigh waves is mathematically modeled by a half-space problem. To simplify the presentation, we will consider the 2-D problems only. First, the domain of interest is the infinite half-space defined by

$$\widehat{\Omega} := \{(x, z) \,|\, -\infty < x < \infty, \, \Gamma(x) < z < \infty\}$$

where $\Gamma(x)$ is a function which models the surface topography. In the domain $\widehat{\Omega}$, we solve the following elastic wave equation

$$\rho \frac{\partial \mathbf{u}}{\partial t} - \operatorname{div} \boldsymbol{\Sigma} = \mathbf{f}, \tag{1}$$

$$\mathbf{A} \frac{\partial \boldsymbol{\Sigma}}{\partial t} - \boldsymbol{\varepsilon}(\mathbf{u}) = 0, \tag{2}$$

where ρ is the density, $\mathbf{u} = (u_1, u_2)^T$ is the velocity field and $\boldsymbol{\Sigma} = (\sigma_{ij})$ is the 2×2 symmetric stress tensor. In addition, $\mathbf{f} = (f_1, f_2)^T$ is a given source term. We write $\boldsymbol{\sigma}_1 = (\sigma_{11}, \sigma_{12})$ and $\boldsymbol{\sigma}_2 = (\sigma_{21}, \sigma_{22})$ as the first and the second rows of $\boldsymbol{\Sigma}$, respectively. The above divergence is defined as $\operatorname{div} \boldsymbol{\Sigma} = (\operatorname{div} \sigma_1, \operatorname{div} \sigma_2)^T$. Moreover, we have $\boldsymbol{\varepsilon}(\mathbf{u})_{ij} = \frac{1}{2}(\partial_i u_j + \partial_j u_i)$. The matrix $\mathbf{A}$ is defined by

$$\mathbf{A} = \begin{pmatrix} \lambda + 2\mu & \lambda & 0 & 0 \\ \lambda & \lambda + 2\mu & 0 & 0 \\ 0 & 0 & 2\mu & 0 \\ 0 & 0 & 0 & 2\mu \end{pmatrix}^{-1}$$

where we assume that $\mathbf{\Sigma} = (\sigma_{11}, \sigma_{22}, \sigma_{12}, \sigma_{21})^T$ in equation 2; λ and μ are the first and second Lamé parameters of the material. Introducing a skew-symmetric 2×2 matrix $\mathbf{\Gamma}$, we have

$$\rho \frac{\partial \mathbf{u}}{\partial t} - \operatorname{div} \mathbf{\Sigma} = \mathbf{f}, \tag{3}$$

$$\mathbf{A} \frac{\partial \sigma}{\partial t} - \nabla \mathbf{u} + \mathbf{\Gamma} = 0, \tag{4}$$

where

$$\mathbf{\Gamma} = (\gamma_{ij}) = \frac{1}{2}(\partial_j u_i - \partial_i u_j).$$

Note that in the 2-D setting, the skew-symmetric matrix $\mathbf{\Gamma}$ is equivalent to a scalar function γ, since the diagonal terms are zero and the off-diagonal terms have the same magnitude with opposite signs. We remark that the role of $\mathbf{\Gamma}$ in the SDG method is a Lagrange multiplier to enforce the symmetry of the approximate stress tensor. The details will be explained in the next section. To solve the above elastic wave equations 3 and 4, we impose suitable initial conditions and the following free-surface boundary condition

$$\mathbf{\Sigma}\, \mathbf{n} = 0 \qquad \text{on } z = \Gamma(x)$$

where $\mathbf{n}$ is the outward normal to the free surface, and $\mathbf{\Sigma}\, \mathbf{n}$ is the standard matrix-vector product.

We introduce some notations that will be used throughout the paper. For two tensors $\mathbf{\Sigma}$ and $\boldsymbol{\alpha}$, we define

$$\mathbf{\Sigma} \cdot \boldsymbol{\alpha} = \sum_{i=1}^{2} \sum_{j=1}^{2} \sigma_{ij} \alpha_{ij}.$$

For a tensor $\mathbf{\Sigma}$ and a vector $\mathbf{u}$, we define

$$\mathbf{\Sigma} \cdot \nabla \mathbf{u} = \sum_{i=1}^{2} \boldsymbol{\sigma}_i \cdot \nabla u_i$$

and

$$\mathbf{u} \cdot (\operatorname{div} \boldsymbol{\Sigma}) = \sum_{i=1}^{2} u_i (\operatorname{div} \boldsymbol{\sigma}_i).$$

For a unit vector $\mathbf{n}$, we define

$$\mathbf{u} \cdot (\boldsymbol{\Sigma}\, \mathbf{n}) = \sum_{i=1}^{2} u_i (\boldsymbol{\sigma}_i \cdot \mathbf{n}).$$

THE SDG METHOD

A staggered triangular grid

We will now present the triangulation of the domain by an unstructured staggered grid. Let Ω be the computational domain, which is a truncation of the infinite half-space $\widehat{\Omega}$ and is defined by

$$\Omega = \{(x, z) \,|\, -R < x < R,\, \Gamma(x) < z < L\}.$$

We assume that Ω is triangulated by an initial triangular mesh, called $\mathcal{T}_h'$. This mesh can be formed by any mesh generator. For each triangle in this mesh, we choose an interior point ν, and then subdivide each triangle into 3 sub-triangles by connecting this point ν to the three vertices of the triangle. A new mesh, called $\mathcal{T}_h$, is then formed by this sub-division process. That is, $\mathcal{T}_h$ is the refined triangulation of $\mathcal{T}_h'$ defined by the above construction. The set of all these nodes ν is denoted by $\mathcal{N}$. An example of such construction is illustrated in Figure 1. The triangles of the initial triangulation $\mathcal{T}_h'$ are denoted by solid lines. The newly formed edges are denoted by dotted lines.

Next, we define two types of macro elements. The first type of macro elements is defined with

respect to the initial mesh. In particular, the triangles of the initial mesh $\mathcal{T}_h'$ are called the first-type macro elements. We use $\mathcal{S}(\nu)$ to denote such a macro element, and we remark that these elements are parametrized by ν. An example of such an element is illustrated by the shaded region with horizontal lines in Figure 1. The second type of macro elements is defined with respect to the edges of the initial triangulation $\mathcal{T}_h'$, and we use $\mathcal{R}(\kappa)$ to denote such a macro element. The macro element $\mathcal{R}(\kappa)$ is defined as the union of the two triangles in $\mathcal{T}_h$ sharing the edge κ. An example of such an element is illustrated by the shaded region with vertical lines in Figure 1. If an edge κ of the initial triangulation lies on the boundary of the computational domain, then we define $\mathcal{R}(\kappa)$ to be the only triangle in $\mathcal{T}_h$ having the edge κ. Moreover, we use the notation $\mathcal{F}_u$ to represent the set of edges of the initial triangulation and $\mathcal{F}_u^0$ the subset of interior edges, as u will be defined to be continuous across those edges. We use the notation $\mathcal{F}_\sigma$ to denote the set of new edges formed by the above sub-division process, as the normal components of σ will be defined to be continuous across those new edges.

Let $m \geq 1$ be a non-negative integer representing the order of polynomials used in our approximation space. For any triangle τ in the triangulation $\mathcal{T}_h$, we let $P^m(\tau)$ be the space of polynomials of degree at most m defined on τ. We define P^m as the space of piecewise $P^m(\tau)$ functions; that is, $v \in P^m$ if the restriction of v on each triangle $\tau \in \mathcal{T}_h$ is in $P^m(\tau)$. We remark that we do not impose any continuity of functions in P_m on the edges of the triangulation $\mathcal{T}_h$.

Next, we present definitions of the approximation spaces. First, we introduce the function space $(U_h)^2$ for the approximation of the velocity vector $\mathbf{u}$. Each component of $\mathbf{u}$ belongs to the space U_h, which is defined by

$$U_h = \{v \in P^m \,|\, v \text{ is continuous on } \mathcal{F}_u^0\}. \tag{5}$$

Thus, the functions in the space U_h are polynomials of at most degree m on each triangle $\tau \in \mathcal{T}_h$ such that they are continuous across the internal edges of the initial triangulation $\mathcal{T}_h'$, namely, the set $\mathcal{F}_u^0$. Since the functions in U_h are in general discontinuous on $\mathcal{F}_\sigma$, these functions are supported on $\mathcal{R}(\kappa)$, the second-type macro element. Second, we introduce the function space $(W_h)^2$ for the approximation of $\boldsymbol{\Sigma}$. Both of the vectors $\boldsymbol{\sigma}_1$ and $\boldsymbol{\sigma}_2$ belong to the space W_h, which is defined by

$$W_h = \{\boldsymbol{\alpha} \in (P^m)^2 \,|\, \boldsymbol{\alpha} \cdot \mathbf{n} \text{ is continuous on } \mathcal{F}_\sigma\}. \tag{6}$$

The vector fields in the space W_h are polynomials of degree at most m on each triangle $\tau \in \mathcal{T}_h$ such that the normal components on the set of edges $\mathcal{F}_\sigma$ are continuous. Since the vector fields in W_h are in general discontinuous on $\mathcal{F}_u^0$, these vectors are supported on $\mathcal{S}(\nu)$, the first-type macro element. Finally, we introduce the function space X_h for the approximation of the function $\boldsymbol{\Gamma}$. We will take $X_h = P^{m-1}$, which contains functions that are discontinuous on all edges in the triangulation $\mathcal{T}_h$.

Derivation

We will now derive the SDG method for the approximation of equations 3 and 4. We consider the first component of equation 3, namely,

$$\rho \frac{\partial u_1}{\partial t} - \operatorname{div} \boldsymbol{\sigma}_1 = f_1. \tag{7}$$

Let v_1 be a smooth test function. Multiplying equation 7 by the test function v_1 and integrating on $\mathcal{R}(\kappa)$ yields

$$\int_{\mathcal{R}(\kappa)} \rho \frac{\partial u_1}{\partial t} v_1 \, dx - \int_{\mathcal{R}(\kappa)} (\operatorname{div} \boldsymbol{\sigma}_1) v_1 \, dx = \int_{\mathcal{R}(\kappa)} f_1 v_1 \, dx. \tag{8}$$

Using integration by parts, we have

$$\int_{\mathcal{R}(\kappa)} \rho \frac{\partial u_1}{\partial t} v_1 \, dx + \int_{\mathcal{R}(\kappa)} \boldsymbol{\sigma}_1 \cdot \nabla v_1 \, dx - \int_{\partial \mathcal{R}(\kappa)} (\boldsymbol{\sigma}_1 \cdot \mathbf{n}) v_1 \, ds = \int_{\mathcal{R}(\kappa)} f_1 v_1 \, dx. \tag{9}$$

Similarly, for the second component of equation 3, we have

$$\int_{\mathcal{R}(\kappa)} \rho \frac{\partial u_2}{\partial t} v_2 \, dx + \int_{\mathcal{R}(\kappa)} \boldsymbol{\sigma}_2 \cdot \nabla v_2 \, dx - \int_{\partial \mathcal{R}(\kappa)} (\boldsymbol{\sigma}_2 \cdot \mathbf{n}) v_2 \, ds = \int_{\mathcal{R}(\kappa)} f_2 v_2 \, dx. \tag{10}$$

Combining the above equations 9 and 10, we have

$$\int_{\mathcal{R}(\kappa)} \rho \frac{\partial \mathbf{u}}{\partial t} \cdot \mathbf{v} \, dx + \int_{\mathcal{R}(\kappa)} \boldsymbol{\Sigma} \cdot \nabla \mathbf{v} \, dx - \int_{\partial \mathcal{R}(\kappa)} (\boldsymbol{\Sigma}\, \mathbf{n}) \cdot \mathbf{v} \, ds = \int_{\mathcal{R}(\kappa)} \mathbf{f} \cdot \mathbf{v} \, dx \tag{11}$$

for all smooth test functions $\mathbf{v} = (v_1, v_2)^T$. We remark that equation 11 holds for all macro elements $\mathcal{R}(\kappa)$ and all test functions $\mathbf{v}$ such that $\mathbf{v} = 0$ on the Dirichlet boundary of the computational domain Ω. We also remark that the above boundary condition for the test function is only applied to the Dirichlet boundary and the boundary where PML is used. This boundary condition is not applied to the free surface and periodic boundary.

Next we consider equation 4. Let $\boldsymbol{\alpha} = (\boldsymbol{\alpha}_1, \boldsymbol{\alpha}_2)^T$ be a smooth 2×2 test tensor, where $\boldsymbol{\alpha}_1$ and $\boldsymbol{\alpha}_2$ are two row vectors. Notice that $\boldsymbol{\alpha}$ is not necessarily symmetric. Multiplying equation 4 by $\boldsymbol{\alpha}$ and integrating on the macro element $\mathcal{S}(\nu)$, we have

$$\int_{\mathcal{S}(\nu)} \mathbf{A} \frac{\partial \boldsymbol{\Sigma}}{\partial t} \cdot \boldsymbol{\alpha} \, dx - \int_{\mathcal{S}(\nu)} \nabla \mathbf{u} \cdot \boldsymbol{\alpha} \, dx + \int_{\mathcal{S}(\nu)} \boldsymbol{\Gamma} \cdot \boldsymbol{\alpha} \, dx = 0. \tag{12}$$

For the gradient term involving $\boldsymbol{\alpha}_1$, we apply integration by parts to get

$$\int_{\mathcal{S}(\nu)} \nabla u_1 \cdot \boldsymbol{\alpha}_1 \, dx = - \int_{\mathcal{S}(\nu)} u_1 \operatorname{div} \boldsymbol{\alpha}_1 \, dx + \int_{\partial \mathcal{S}(\nu)} u_1 \, (\boldsymbol{\alpha}_1 \cdot \mathbf{n}) \, ds. \tag{13}$$

Similarly, for the gradient term involving $\boldsymbol{\alpha}_2$, we have

$$\int_{\mathcal{S}(\nu)} \nabla u_2 \cdot \boldsymbol{\alpha}_2 \, dx = - \int_{\mathcal{S}(\nu)} u_2 \operatorname{div} \boldsymbol{\alpha}_2 \, dx + \int_{\partial \mathcal{S}(\nu)} u_2 \, (\boldsymbol{\alpha}_2 \cdot \mathbf{n}) \, ds. \tag{14}$$

Hence, using equations 13 and 14, we have

$$\int_{\mathcal{S}(\nu)} \mathbf{A}\frac{\partial \boldsymbol{\Sigma}}{\partial t} \cdot \boldsymbol{\alpha}\, dx + \int_{\mathcal{S}(\nu)} \mathbf{u}\, \mathrm{div}\, \boldsymbol{\alpha}\, dx - \int_{\partial \mathcal{S}(\nu)} \mathbf{u} \cdot (\boldsymbol{\alpha}\, \mathbf{n})\, ds + \int_{\mathcal{S}(\nu)} \boldsymbol{\Gamma} \cdot \boldsymbol{\alpha}\, dx = 0. \tag{15}$$

Now, we will present the definition of the SDG method. The approximations of $\mathbf{u}$, $\boldsymbol{\Sigma}$ and $\boldsymbol{\Gamma}$ are denoted by $\mathbf{u}_h$, $\boldsymbol{\Sigma}_h$ and $\boldsymbol{\Gamma}_h$ and are obtained in the spaces $(U_h)^2, (W_h)^2$ and X_h, respectively. For any macro element $\mathcal{R}(\kappa)$, equation 11 suggests the following approximation

$$\int_{\mathcal{R}(\kappa)} \rho \frac{\partial \mathbf{u}_h}{\partial t} \cdot \mathbf{v}\, dx + \int_{\mathcal{R}(\kappa)} \boldsymbol{\Sigma}_h \cdot \nabla \mathbf{v}\, dx - \int_{\partial \mathcal{R}(\kappa)} (\boldsymbol{\Sigma}_h\, \mathbf{n}) \cdot \mathbf{v}\, ds = \int_{\mathcal{R}(\kappa)} \mathbf{f} \cdot \mathbf{v}\, dx, \tag{16}$$

for any test function v in the space $(U_h)^2$. Summing over all $\mathcal{R}(\kappa)$, we have

$$\int_{\Omega} \rho \frac{\partial \mathbf{u}_h}{\partial t} \cdot \mathbf{v}\, dx + \sum_{\kappa \in \mathcal{F}_u} \Big(\int_{\mathcal{R}(\kappa)} \boldsymbol{\Sigma}_h \cdot \nabla \mathbf{v}\, dx - \int_{\partial \mathcal{R}(\kappa)} (\boldsymbol{\Sigma}_h\, \mathbf{n}) \cdot \mathbf{v}\, ds \Big) = \int_{\Omega} \mathbf{f} \cdot \mathbf{v}\, dx, \quad \forall \mathbf{v} \in (U_h)^2. \tag{17}$$

For any macro element $\mathcal{S}(\nu)$, equation 15 suggests the following approximation

$$\int_{\mathcal{S}(\nu)} \mathbf{A}\frac{\partial \boldsymbol{\Sigma}_h}{\partial t} \cdot \boldsymbol{\alpha}\, dx + \int_{\mathcal{S}(\nu)} \mathbf{u}_h\, \mathrm{div}\, \boldsymbol{\alpha}\, dx - \int_{\partial \mathcal{S}(\nu)} \mathbf{u}_h \cdot (\boldsymbol{\alpha}\, \mathbf{n})\, ds + \int_{\mathcal{S}(\nu)} \boldsymbol{\Gamma}_h \cdot \boldsymbol{\alpha}\, dx = 0, \tag{18}$$

for any test function $\boldsymbol{\alpha}$ in the space $(W_h)^2$. Summing over all $\mathcal{S}(\nu)$, we have

$$\int_{\Omega} \mathbf{A}\frac{\partial \boldsymbol{\Sigma}_h}{\partial t} \cdot \boldsymbol{\alpha}\, dx + \sum_{\nu \in \mathcal{N}} \Big(\int_{\mathcal{S}(\nu)} \mathbf{u}_h\, \mathrm{div}\, \boldsymbol{\alpha}\, dx - \int_{\partial \mathcal{S}(\nu)} \mathbf{u}_h \cdot (\boldsymbol{\alpha}\, \mathbf{n})\, ds \Big) + \int_{\Omega} \boldsymbol{\Gamma}_h \cdot \boldsymbol{\alpha}\, dx = 0, \quad \forall \boldsymbol{\alpha} \in (W_h)^2. \tag{19}$$

In addition, we will impose the following weak symmetry condition for $\boldsymbol{\Sigma}_h$

$$\int_{\Omega} \boldsymbol{\Sigma}_h \cdot \boldsymbol{\eta}\, dx = 0, \quad \forall \boldsymbol{\eta} \in X_h. \tag{20}$$

Equations 17, 19 and 20 give the definition of our SDG method. Throughout the paper, we write $\mathbf{u}_h = (\mathbf{u}_{h,1}, \mathbf{u}_{h,2})^T$ and $\boldsymbol{\Sigma}_h = (\boldsymbol{\sigma}_{h,1}, \boldsymbol{\sigma}_{h,2})^T$, where $\boldsymbol{\Sigma}_{h,i}$ is the i-th row of $\boldsymbol{\Sigma}_h$.

Next, we will derive the linear system arising from equations 17, 19 and 20. Assume that the dimensions of U_h, W_h and X_h are m_U, m_W and m_X, respectively. Let $\{v^{(i)}\}_{i=1}^{m_U}$ be the basis

functions of U_h, $\{\boldsymbol{\alpha}^{(i)}\}_{i=1}^{m_W}$ be the basis functions of W_h, and $\{\boldsymbol{\eta}^{(i)}\}_{i=1}^{m_X}$ be the basis functions of X_h.

Each component of $\mathbf{u}_h$ can be represented by

$$\mathbf{u}_{h,k} = \sum_{i=1}^{m_U} u_{h,k}^{(i)}\, v^{(i)}, \qquad k = 1, 2. \tag{21}$$

Moreover, each row of $\boldsymbol{\Sigma}_h$ can be represented by

$$\boldsymbol{\sigma}_{h,k} = \sum_{i=1}^{m_W} \sigma_{h,k}^{(i)}\, \boldsymbol{\alpha}^{(i)}, \qquad k = 1, 2. \tag{22}$$

Similarly, $\boldsymbol{\Gamma}_h$ can be represented by

$$\boldsymbol{\Gamma}_h = \sum_{i=1}^{m_X} \gamma_h^{(i)}\, \boldsymbol{\eta}^{(i)}. \tag{23}$$

We define the $m_U \times m_U$ mass matrix $\mathbf{M}_u$ by

$$(\mathbf{M}_u)_{ij} = \int_\Omega \rho\, v^{(i)}\, v^{(j)}\, dx. \tag{24}$$

Notice that the basis functions of $(W_h)^2$ have the form $\boldsymbol{\beta}^{(i)} = (\boldsymbol{\alpha}^{(i)}, 0)^T$ or $\boldsymbol{\beta}^{(i)} = (0, \boldsymbol{\alpha}^{(i)})^T$. Thus, we define the $2m_W \times 2m_W$ mass matrix $\mathbf{M}_\sigma$ by

$$(\mathbf{M}_\sigma)_{ij} = \int_\Omega (\mathbf{A}\boldsymbol{\beta}^{(i)}) \cdot \boldsymbol{\beta}^{(j)}\, dx. \tag{25}$$

We also define the $2m_W \times m_X$ matrix $\mathbf{C}_\gamma$ by

$$(\mathbf{C}_\gamma)_{ij} = \int_\Omega \boldsymbol{\beta}^{(i)} \cdot \boldsymbol{\eta}^{(j)}\, dx. \tag{26}$$

Moreover, with $v^{(i)} \in U_h$ and $\alpha^{(j)} \in W_h$, we define the following $m_U \times m_W$ matrix $\mathbf{B}$ by

$$\mathbf{B}_{ij} = \sum_{\kappa \in \mathcal{F}_u} \left(\int_{\mathcal{R}(\kappa)} \boldsymbol{\alpha}^{(j)} \cdot \nabla \mathbf{v}^{(i)}\, dx - \int_{\partial\mathcal{R}(\kappa)} (\boldsymbol{\alpha}^{(j)} \cdot n)\, \mathbf{v}^{(i)}\, ds \right) \tag{27}$$

and the following $m_W \times m_U$ matrix B^* by

$$\mathbf{B}_{ji}^* = -\sum_{\nu \in \mathcal{N}} \left(\int_{\mathcal{S}(\nu)} \mathbf{v}^{(i)}\, \mathrm{div}\, \boldsymbol{\alpha}^{(j)}\, dx - \int_{\partial\mathcal{S}(\nu)} \mathbf{v}^{(i)}\, (\boldsymbol{\alpha}^{(j)} \cdot \mathbf{n})\, ds \right). \tag{28}$$

Finally, we define the following two $m_U \times 1$ vectors $\vec{\mathbf{f}}_k = (f_k^{(i)})$ by

$$f_k^{(i)} = \int_\Omega f_k v^{(i)}\, dx, \quad k = 1, 2. \tag{29}$$

Let $\vec{\mathbf{u}}_1 = (u_{h,1}^{(i)})$ and $\vec{\mathbf{u}}_2 = (u_{h,2}^{(i)})$ be vectors of coefficients giving the approximate solutions $u_{h,1}$ and $u_{h,2}$ in equation 21. Moreover, we let $\vec{\boldsymbol{\sigma}}_1 = (\sigma_{h,1}^{(i)})$ and $\vec{\boldsymbol{\sigma}}_2 = (\sigma_{h,2}^{(i)})$ be vectors of coefficients giving the approximate solutions $\boldsymbol{\sigma}_{h,1}$ and $\boldsymbol{\sigma}_{h,2}$ in equation 22. We write $\vec{\boldsymbol{\sigma}} = (\vec{\boldsymbol{\sigma}}_1, \vec{\boldsymbol{\sigma}}_2)^T$. Finally, we let $\vec{\boldsymbol{\gamma}} = (\gamma_h^{(i)})$ be the vector of coefficients giving the approximate solutions $\boldsymbol{\Gamma}_h$ in equation 23. Using these definitions, equation 17 can be written as

$$\frac{d}{dt}\mathbf{M}_u\vec{\mathbf{u}}_1 + \mathbf{B}\vec{\boldsymbol{\sigma}}_1 = \vec{\mathbf{f}}_1, \quad \frac{d}{dt}\mathbf{M}_u\vec{\mathbf{u}}_2 + \mathbf{B}\vec{\boldsymbol{\sigma}}_2 = \vec{\mathbf{f}}_2. \tag{30}$$

Moreover, equation 19 can be written as

$$\frac{d}{dt}(\mathbf{M}_\sigma\vec{\boldsymbol{\sigma}}) - \begin{pmatrix} \mathbf{B}^* & 0 \\ 0 & \mathbf{B}^* \end{pmatrix} \begin{pmatrix} \vec{\mathbf{u}}_1 \\ \vec{\mathbf{u}}_2 \end{pmatrix} + \mathbf{C}_\gamma\vec{\boldsymbol{\gamma}} = 0. \tag{31}$$

Finally, equation 20 can be written as

$$\mathbf{C}_\gamma^T\vec{\boldsymbol{\sigma}} = 0. \tag{32}$$

Equations 30, 31 and 32 define the linear system for the SDG method. We remark that matrix $\mathbf{B}^*$ is the transpose of the matrix $\mathbf{B}$, which is proved in Chung and Engquist (2009). We also remark that the convergence of our method can be proved using techniques in Chung and Engquist (2009) and Stenberg (1988).

Time discretization

For time discretization, we will apply the standard leap-frog scheme. The velocity field $\vec{\mathbf{u}}$ is computed at the times $t_n = n\Delta t$ while the stress tensors $\vec{\boldsymbol{\Sigma}}$ and $\vec{\boldsymbol{\gamma}}$ are computed at $t_{n+\frac{1}{2}} = (n + \frac{1}{2})\Delta t$,

where Δt is the time step size and n is a non-negative integer. We will use $\vec{\mathbf{u}}^n$ to denote the approximate value of $\vec{\mathbf{u}}$ at time t_n. Moreover, we will use $\vec{\mathbf{\Sigma}}^{n+\frac{1}{2}}$ and $\vec{\boldsymbol{\gamma}}^{n+\frac{1}{2}}$ to denote the approximate values of $\vec{\mathbf{\Sigma}}$ and $\vec{\boldsymbol{\gamma}}$ at time $t_{n+\frac{1}{2}}$, respectively.

For equation 30, we use the central difference approximation in time at $t_{n+\frac{1}{2}}$ to obtain the following approximation

$$\mathbf{M}_u \frac{\vec{\mathbf{u}}_1^{n+1} - \vec{\mathbf{u}}_1^n}{\Delta t} + \mathbf{B}\vec{\boldsymbol{\sigma}}_1^{n+\frac{1}{2}} = \vec{\mathbf{f}}_1^{n+\frac{1}{2}}, \quad \mathbf{M}_u \frac{\vec{\mathbf{u}}_2^{n+1} - \vec{\mathbf{u}}_2^n}{\Delta t} + \mathbf{B}\vec{\boldsymbol{\sigma}}_2^{n+\frac{1}{2}} = \vec{\mathbf{f}}_2^{n+\frac{1}{2}}. \tag{33}$$

On the other hand, we evaluate equations 31 and 32 at the time t_n and use the central difference approximation for the time derivative to obtain the following

$$\begin{aligned} \mathbf{M}_\sigma \frac{\vec{\boldsymbol{\sigma}}^{n+\frac{3}{2}} - \vec{\boldsymbol{\sigma}}^{n+\frac{1}{2}}}{\Delta t} - \widetilde{\mathbf{B}}^* \vec{\mathbf{u}}^{n+1} + \mathbf{C}_\gamma \frac{\vec{\boldsymbol{\gamma}}^{n+\frac{3}{2}} + \vec{\boldsymbol{\gamma}}^{n+\frac{1}{2}}}{2} &= 0 \\ \mathbf{C}_\gamma^T \vec{\boldsymbol{\sigma}}^{n+\frac{3}{2}} &= 0 \end{aligned} \tag{34}$$

where

$$\widetilde{\mathbf{B}}^* = \begin{pmatrix} \mathbf{B}^* & 0 \\ 0 & \mathbf{B}^* \end{pmatrix}.$$

Equation 34 can be written as the following saddle point system

$$\begin{aligned} \frac{2}{\Delta t}\mathbf{M}_\sigma \vec{\mathbf{\Sigma}}^{n+\frac{3}{2}} + \mathbf{C}_\gamma \vec{\boldsymbol{\gamma}}^{n+\frac{3}{2}} = \frac{2}{\Delta t}\mathbf{M}_\sigma \vec{\boldsymbol{\sigma}}^{n+\frac{1}{2}} - \mathbf{C}_\gamma \vec{\boldsymbol{\gamma}}^{n+\frac{1}{2}} + 2\widetilde{\mathbf{B}}^* \vec{\mathbf{u}}^{n+1} &:= \vec{\mathbf{r}}^{n+\frac{1}{2}} \\ \mathbf{C}_\gamma^T \vec{\boldsymbol{\sigma}}^{n+\frac{3}{2}} = 0. & \end{aligned} \tag{35}$$

Equations 33 and 35 define the time-marching formula. In particular, for any given $\vec{\mathbf{u}}^n$, $\vec{\boldsymbol{\sigma}}^{n+\frac{1}{2}}$ and $\vec{\boldsymbol{\gamma}}^{n+\frac{1}{2}}$, where $n = 0, 1, 2 \cdots$, we can use equation 33 to obtain $\vec{\mathbf{u}}^{n+1}$. Then using the newly obtained $\vec{\mathbf{u}}^{n+1}$, and current values of $\vec{\boldsymbol{\sigma}}^{n+\frac{1}{2}}$ and $\vec{\boldsymbol{\gamma}}^{n+\frac{1}{2}}$, we can use equation 35 to obtain approximations $\vec{\boldsymbol{\sigma}}^{n+\frac{3}{2}}$ and $\vec{\boldsymbol{\gamma}}^{n+\frac{3}{2}}$.

Although equation 35 is a coupled system with respect to the unknowns $\vec{\boldsymbol{\sigma}}^{n+\frac{3}{2}}$ and $\vec{\boldsymbol{\gamma}}^{n+\frac{3}{2}}$, it can be solved in the following element-wise manner. Since the mass matrix $\mathbf{M}_\sigma$ and the matrix $\mathbf{C}_\gamma$ are

block diagonal, namely,

$$\mathbf{M}_\sigma = \begin{pmatrix} \mathbf{M}_\sigma^{\mathcal{S}(\nu_1)} & & & \\ & \mathbf{M}_\sigma^{\mathcal{S}(\nu_2)} & & \\ & & \ddots & \\ & & & \mathbf{M}_\sigma^{\mathcal{S}(\nu_N)} \end{pmatrix} \text{ and } \mathbf{C}_\gamma = \begin{pmatrix} \mathbf{C}_\gamma^{\mathcal{S}(\nu_1)} & & & \\ & \mathbf{C}_\gamma^{\mathcal{S}(\nu_2)} & & \\ & & \ddots & \\ & & & \mathbf{C}_\gamma^{\mathcal{S}(\nu_N)} \end{pmatrix}$$

where N is the number of triangles in the initial triangulation $\mathcal{T}_h'$, $\mathbf{M}_\sigma^{\mathcal{S}(\nu_i)}$ is the local mass matrix corresponding to the macro element $\mathcal{S}(\nu_i)$ and $\mathbf{C}_\gamma^{\mathcal{S}(\nu_i)}$ is the restriction of $\mathbf{C}_\gamma$ to the components corresponding to the macro element $\mathcal{S}(\nu_i)$, equation 35 can be solved as

$$\begin{aligned} \frac{2}{\Delta t}\mathbf{M}_\sigma^{\mathcal{S}(\nu_i)}\vec{\boldsymbol{\sigma}}^{n+\frac{3}{2}} + \mathbf{C}_\gamma^{\mathcal{S}(\nu_i)}\vec{\boldsymbol{\gamma}}^{n+\frac{3}{2}} &= \vec{\mathbf{r}}^{n+\frac{1}{2}} \\ (\mathbf{C}_\gamma^{\mathcal{S}(\nu_i)})^T\vec{\boldsymbol{\sigma}}^{n+\frac{3}{2}} &= 0 \end{aligned} \tag{36}$$

where $\vec{\boldsymbol{\sigma}}^{n+\frac{3}{2}}$, $\vec{\boldsymbol{\gamma}}^{n+\frac{3}{2}}$ and $\vec{\mathbf{r}}^{n+\frac{1}{2}}$ are understood as the restriction to the components corresponding to the macro element $\mathcal{S}(\nu_i)$. Similarly, the mass matrix $\mathbf{M}_u$ is also block diagonal, namely,

$$\mathbf{M}_u = \begin{pmatrix} \mathbf{M}_u^{\mathcal{R}(\kappa_1)} & & & \\ & \mathbf{M}_u^{\mathcal{R}(\kappa_2)} & & \\ & & \ddots & \\ & & & \mathbf{M}_u^{\mathcal{R}(\kappa_F)} \end{pmatrix}$$

where F is the number of second type macro elements, which is the same as the number of edges in the initial triangulation $\mathcal{T}_h'$. Therefore, equation 33 can be solved element-by-element as well.

The system defined in equation 36 is invertible. From the classical theory of saddle point problem, we need to show that, for every $\eta \in X_h$, there exists $\boldsymbol{\alpha} \in (W_h)^2$ such that

$$\int_\Omega (\alpha_{12} - \alpha_{21})\eta \, dx := \int_\Omega \boldsymbol{\alpha} \cdot \boldsymbol{\eta} \, dx = \int_\Omega \eta^2 \, dx \tag{37}$$

and

$$\int_\Omega \mathbf{A}\boldsymbol{\alpha}\cdot\boldsymbol{\alpha}\,dx \le K_0\int_\Omega \eta^2\,dx \tag{38}$$

where α_{12} is the second component of $\boldsymbol{\alpha}_1 \in W_h$, α_{21} is the first component of $\boldsymbol{\alpha}_2 \in W_h$ and $K_0 > 0$ is a constant independent of the mesh size. Consider a triangle $\tau \in \mathcal{T}_h$. From the theory in the paper Chung and Engquist (2009), we can find a unique $\boldsymbol{\alpha}_1$ satisfying

$$\begin{aligned}
&\boldsymbol{\alpha}_1\cdot\mathbf{n} = 0, \qquad \text{on } \kappa \in \partial\tau \cap \mathcal{F}_\sigma\\
&\int_\tau \alpha_{11}\eta\,dx = 0\\
&\int_\tau \alpha_{11}\eta\,dx = \frac{1}{2}\int_\tau \eta^2\,dx.
\end{aligned}$$

Similarly, we can find a unique α_2 satisfying

$$\begin{aligned}
&\boldsymbol{\alpha}_2\cdot n = 0, \qquad \text{on } \kappa \in \partial\tau \cap \mathcal{F}_\sigma\\
&\int_\tau \alpha_{21}\eta\,dx = -\frac{1}{2}\int_\tau \eta^2\,dx\\
&\int_\tau \alpha_{22}\eta\,dx = 0.
\end{aligned}$$

Note that, the above constructions can be done on each $\tau \in \mathcal{T}_h$ without destroying the continuity conditions in the space W_h. Finally, from the above construction, we can see easily that (37) and (38) hold.

Numerical stability

We will now derive a sufficient condition on the size of Δt for the stability of the SDG method in equations 33 and 34. We will assume that the source term $\mathbf{f} = 0$ to simplify the calculations, and we remark that the same steps can be used to show stability of the method when $\mathbf{f} \neq 0$. First,

multiplying equation 33 by $\vec{\mathbf{u}}^{n+1} + \vec{\mathbf{u}}^n$, we obtain for $k = 1, 2$,

$$\left(\mathbf{M}_u \frac{\vec{\mathbf{u}}_k^{n+1} - \vec{\mathbf{u}}_k^n}{\Delta t}, \vec{\mathbf{u}}_k^{n+1} + \vec{\mathbf{u}}_k^n\right) + \left(\mathbf{B}\vec{\boldsymbol{\sigma}}_k^{n+\frac{1}{2}}, \vec{\mathbf{u}}_k^{n+1} + \vec{\mathbf{u}}_k^n\right) = \left(\mathbf{f}_k^{n+\frac{1}{2}}, \vec{\mathbf{u}}_k^{n+1} + \vec{\mathbf{u}}_k^n\right). \tag{39}$$

Moreover, multiplying equation 34 by $\vec{\boldsymbol{\sigma}}^{n+\frac{3}{2}} + \vec{\boldsymbol{\sigma}}^{n+\frac{1}{2}}$, we obtain

$$\left(\mathbf{M}_\sigma \frac{\vec{\boldsymbol{\sigma}}^{n+\frac{3}{2}} - \vec{\boldsymbol{\sigma}}^{n+\frac{1}{2}}}{\Delta t}, \vec{\boldsymbol{\sigma}}^{n+\frac{3}{2}} + \vec{\boldsymbol{\sigma}}^{n+\frac{1}{2}}\right) - \left(\widetilde{\mathbf{B}}^* \vec{\mathbf{u}}^{n+1}, \vec{\boldsymbol{\sigma}}^{n+\frac{3}{2}} + \vec{\boldsymbol{\sigma}}^{n+\frac{1}{2}}\right) = 0 \tag{40}$$

By the fact that $\mathbf{B}^* = \mathbf{B}^T$ which is proved in Chung and Engquist (2009) and the definition of $\widetilde{\mathbf{B}}^*$, we have

$$\begin{aligned}
&\left(\mathbf{B}\vec{\boldsymbol{\sigma}}_1^{n+\frac{1}{2}}, \vec{\mathbf{u}}_1^n\right) + \left(\mathbf{B}\vec{\boldsymbol{\sigma}}_2^{n+\frac{1}{2}}, \vec{\mathbf{u}}_2^n\right) - \left(\widetilde{\mathbf{B}}^* \vec{\mathbf{u}}^n, \vec{\boldsymbol{\sigma}}^{n+\frac{1}{2}}\right) \\
&= \left(\vec{\boldsymbol{\sigma}}_1^{n+\frac{1}{2}}, \mathbf{B}^T \vec{\mathbf{u}}_1^n\right) + \left(\vec{\boldsymbol{\sigma}}_2^{n+\frac{1}{2}}, \mathbf{B}^T \vec{\mathbf{u}}_2^n\right) - \left(\widetilde{\mathbf{B}}^* \vec{\mathbf{u}}^n, \vec{\boldsymbol{\sigma}}^{n+\frac{1}{2}}\right) \\
&= \left(\vec{\boldsymbol{\sigma}}_1^{n+\frac{1}{2}}, \mathbf{B}^* \vec{\mathbf{u}}_1^n\right) + \left(\vec{\boldsymbol{\sigma}}_2^{n+\frac{1}{2}}, \mathbf{B}^* \vec{\mathbf{u}}_2^n\right) - \left(\widetilde{\mathbf{B}}^* \vec{\mathbf{u}}^n, \vec{\boldsymbol{\sigma}}^{n+\frac{1}{2}}\right) \\
&= 0.
\end{aligned} \tag{41}$$

Let $N > 1$ be a fixed integer. Summing equations 39 and 40 from $n = 0$ to $n = N - 1$ and using equation 41, we have

$$E^N = E^0 + \frac{\Delta t}{2}\left(\widetilde{\mathbf{B}}\vec{\boldsymbol{\sigma}}^{N+\frac{1}{2}}, \vec{\mathbf{u}}^N\right) - \frac{\Delta t}{2}\left(\vec{\boldsymbol{\sigma}}^{\frac{1}{2}}, \widetilde{\mathbf{B}}^* \vec{\mathbf{u}}^0\right), \tag{42}$$

where

$$E^n := \frac{1}{2}\left(\|\vec{\mathbf{u}}_1^n\|_{\mathbf{M}_u}^2 + \|\vec{\mathbf{u}}_2^n\|_{\mathbf{M}_u}^2 + \left\|\vec{\boldsymbol{\sigma}}^{n+\frac{1}{2}}\right\|_{\mathbf{M}_\sigma}^2\right),$$

and the norms above are defined as

$$\|\vec{\mathbf{u}}_k^n\|_{\mathbf{M}_u}^2 = (\mathbf{M}_u \vec{\mathbf{u}}_k^n, \vec{\mathbf{u}}_k^n), \quad k = 1, 2; \qquad \left\|\vec{\boldsymbol{\sigma}}^{n+\frac{1}{2}}\right\|_{\mathbf{M}_\sigma}^2 = (\mathbf{M}_\sigma \vec{\boldsymbol{\sigma}}^{n+\frac{1}{2}}, \vec{\boldsymbol{\sigma}}^{n+\frac{1}{2}}).$$

Let $\mathbf{K} := \widetilde{\mathbf{M}}_u^{-\frac{1}{2}} \widetilde{\mathbf{B}} \mathbf{M}_\sigma^{-\frac{1}{2}}$, where

$$\widetilde{\mathbf{M}}_u = \begin{pmatrix} \mathbf{M}_u & 0 \\ 0 & \mathbf{M}_u \end{pmatrix}.$$

By the Cauchy-Schwarz inequality, we have

$$\left(\widetilde{\mathbf{B}}\vec{\boldsymbol{\sigma}}^{N+\frac{1}{2}}, \vec{\mathbf{u}}^{N}\right) \leq \|\mathbf{K}\|_2 \left\|\vec{\mathbf{u}}^{N}\right\|_{\widetilde{\mathbf{M}}_u} \left\|\vec{\boldsymbol{\sigma}}^{N+\frac{1}{2}}\right\|_{\mathbf{M}_\sigma}, \tag{43}$$

where

$$\left\|\vec{\mathbf{u}}^{N}\right\|^2_{\widetilde{\mathbf{M}}_u} = \left\|\vec{\mathbf{u}}_1^{N}\right\|^2_{\mathbf{M}_u} + \left\|\vec{\mathbf{u}}_2^{N}\right\|^2_{\mathbf{M}_u}.$$

We will now show that the SDG method is stable if $\Lambda := \Delta t \|\mathbf{K}\|_2 < 2$. Using this assumption, equation 42 can be written as

$$E^N \leq E^0 + \frac{\Lambda}{2}\left\|\vec{\mathbf{u}}^{N}\right\|_{\widetilde{\mathbf{M}}_u} \left\|\vec{\boldsymbol{\sigma}}^{N+\frac{1}{2}}\right\|_{\mathbf{M}_\sigma} + \frac{\Lambda}{2}\left\|\vec{\mathbf{u}}^{0}\right\|_{\widetilde{\mathbf{M}}_u} \left\|\vec{\boldsymbol{\sigma}}^{\frac{1}{2}}\right\|_{\mathbf{M}_\sigma}$$

which becomes

$$E^N \leq E^0 + \frac{\Lambda}{4}\Big(\left\|\vec{\mathbf{u}}^{N}\right\|^2_{\widetilde{\mathbf{M}}_u} + \left\|\vec{\boldsymbol{\sigma}}^{N+\frac{1}{2}}\right\|^2_{\mathbf{M}_\sigma} \Big) + \frac{\Lambda}{4}\Big(\left\|\vec{\mathbf{u}}^{0}\right\|^2_{\widetilde{\mathbf{M}}_u} + \left\|\vec{\boldsymbol{\sigma}}^{\frac{1}{2}}\right\|^2_{\mathbf{M}_\sigma} \Big).$$

Hence, we have

$$E^N \leq \frac{1+\frac{\Lambda}{2}}{1-\frac{\Lambda}{2}} E^0$$

provided $1 - \Lambda/2 > 0$. The above inequality gives the stability of the SDG method since $\Lambda < 2$. To find the explicit form of $\|\mathbf{K}\|_2$, it is known that $\|\mathbf{K}\|_2$ is proportional to h^{-1}, where h is the mesh size, since the operator $\mathbf{K}$ is a discrete first order derivative operator. Thus we can write

$$\|\mathbf{K}\|_2 = Ch^{-1} \tag{44}$$

for some constant C. The value of C can be found by computing $\|\mathbf{K}\|_2$ for different values of h and by using a least-squares fitting.

Construction of basis functions

We will present the construction of basis functions in this section. First, we describe the basis functions for U_h. By definition, a function $v \in U_h$ is a polynomial of degree $m \geq 1$ on each triangle $\tau \in \mathcal{T}_h$ and is continuous on the edges $\kappa \in \mathcal{F}_u^0$. Thus, v is decoupled along the boundaries of the second-type macro elements $\mathcal{R}(\kappa)$ for all $\kappa \in \mathcal{F}_u$. Therefore, the basis functions for the space U_h are constructed locally on $\mathcal{R}(\kappa)$. We will consider an interior edge $\kappa \in \mathcal{F}_u^0$ and discuss the corresponding construction of basis functions on $\mathcal{R}(\kappa)$. The case that κ belongs to the boundary of the computational domain can be constructed in the same way. With reference to Figure 1, we will need piecewise polynomials of degree m that are continuous on κ. Thus, the basis functions can be taken as the standard conforming finite element basis functions applied to the domain $\mathcal{R}(\kappa)$ with a triangulation composed of two triangles. Secondly, for the space X_h, the basis functions can be taken as Lagrange basis functions on each triangle in $\mathcal{T}_h$, since there is no continuity requirement.

Finally, we describe the construction of the basis functions for the space W_h. By definition, a vector $\alpha \in W_h$ is a vector polynomial on each triangle $\tau \in \mathcal{T}_h$ with continuous normal components on the edges $\kappa \in \mathcal{F}_\sigma$. Thus, α is decoupled along the boundaries of the first-type macro elements $\mathcal{S}(\nu)$ for all $\nu \in \mathcal{N}$. Therefore, the basis functions for the space W_h are constructed locally on $\mathcal{S}(\nu)$. We will now present a convenient way to construct these functions. Consider a first-type macro element $\mathcal{S}(\nu)$. Let P_1, P_2, P_3 be the three vertices of $\mathcal{S}(\nu)$ and $P_4 = \nu$, which is the point chosen for the subdivision process required by the SDG method; see Figure 2. The corresponding three sub-triangles are denoted by $\tau_1 = P_2P_3P_4$, $\tau_2 = P_1P_3P_4$ and $\tau_3 = P_1P_2P_4$. Moreover, for each of the three edges P_kP_4, $(k = 1, 2, 3)$, in the interior of $\mathcal{S}(\nu)$, we define a region ω_k by the union of the two

sub-triangles having the edge P_kP_4. That is, $\omega_1 = \tau_2 \cup \tau_3$, $\omega_2 = \tau_1 \cup \tau_3$ and $\omega_3 = \tau_1 \cup \tau_2$. In addition, we use $\mathbf{n}_k$, $k = 1, 2, 3$, to denote a fixed unit normal vector for the edges P_kP_4. The basis functions are divided into three types, and each of these three types of basis functions is supported in ω_1, ω_2, and ω_3, respectively. We will present the construction of basis function for the first type, namely those basis functions having support in ω_1. The other two types can be constructed similarly. For the first type of basis functions α, we impose the following conditions

$$\boldsymbol{\alpha} \cdot \mathbf{n}_2 = 0, \text{ on } P_2P_4; \quad \boldsymbol{\alpha} \cdot \mathbf{n}_3 = 0, \text{ on } P_3P_4,$$

that is, $\boldsymbol{\alpha}$ has zero normal component on the edges P_2P_4 and P_3P_4. To obtain the above condition, we require $\boldsymbol{\alpha} \cdot \mathbf{n}_2$ to be identically zero on ω_2 and $\boldsymbol{\alpha} \cdot \mathbf{n}_3$ to be identically zero on ω_3. Notice that, using this construction, we have $\boldsymbol{\alpha} \cdot \mathbf{n}_2$ and $\boldsymbol{\alpha} \cdot n_3$ are identically zero on τ_1, since τ_1 is the intersection of ω_2 and ω_3. Next, we recall that the space W_h requires that $\alpha \cdot \mathbf{n}_1$ be continuous on P_1P_4. We now consider ω_1 and define $\alpha \cdot n_1$ to be a polynomial of degree m in each sub-triangle of ω_1 such that $\alpha \cdot \mathbf{n}_1$ is continuous on P_1P_4. Similar to the construction of basis functions for the space U_h, we now choose basis functions of $\alpha \cdot \mathbf{n}_1$ on ω_1 to be the classical conforming finite element basis functions defined in the domain ω_1 corresponding to the triangulation $\omega_1 = \tau_2 \cup \tau_3$. The construction of basis function is now completed. Since both $\boldsymbol{\alpha} \cdot \mathbf{n}_1$ and $\alpha \cdot \mathbf{n}_3$ are specified in τ_2, the vector $\boldsymbol{\alpha}$ in τ_2 can be re-constructed. Similarly, both $\boldsymbol{\alpha} \cdot \mathbf{n}_1$ and $\boldsymbol{\alpha} \cdot \mathbf{n}_2$ are specified in τ_3 so that the vector $\boldsymbol{\alpha}$ can be re-constructed. Specifically, we can then write

$$\boldsymbol{\alpha}(x) \cdot \mathbf{n}_1 = \begin{cases} g_2(x) & \text{in } \tau_2 \\ \\ g_3(x) & \text{in } \tau_3 \end{cases}$$

where g_2 and g_3 are polynomials of degree m chosen in the way explained above. On τ_2, we have

$\boldsymbol{\alpha} \cdot \mathbf{n}_1 = g_2$ and $\boldsymbol{\alpha} \cdot \mathbf{n}_3 = 0$. Hence, we have on τ_2,

$$\boldsymbol{\alpha} = \frac{g_2}{1 - (\mathbf{n}_1 \cdot \mathbf{n}_3)^2}\mathbf{n}_1 - \frac{(\mathbf{n}_1 \cdot \mathbf{n}_3)g_2}{1 - (\mathbf{n}_1 \cdot \mathbf{n}_3)^2}\mathbf{n}_3.$$

Similarly, we have on τ_3,

$$\boldsymbol{\alpha} = \frac{g_3}{1 - (\mathbf{n}_1 \cdot \mathbf{n}_2)^2}\mathbf{n}_1 - \frac{(\mathbf{n}_1 \cdot \mathbf{n}_2)g_3}{1 - (\mathbf{n}_1 \cdot \mathbf{n}_2)^2}\mathbf{n}_2.$$

In Figure 3, plots of the first type of basis functions for the case $m = 1$ are shown. Notice that, these basis functions have support in ω_1. Moreover, since $m = 1$, there are only 4 distinct basis functions. In particular, ω_1 is the union of two sub-triangles τ_2 and τ_3. By the above construction, we need basis functions for $\boldsymbol{\alpha} \cdot \mathbf{n}_1$ that are linear in each of τ_2 and τ_3, and are continuous on P_1P_4. Thus, we see that there are only 4 choices, by taking $\boldsymbol{\alpha} \cdot \mathbf{n}_1$ equal to one at one of the four vertices of ω_1 and zero at the other three vertices.

NUMERICAL RESULTS

In this section, we present some numerical results to show the performance of the SDG method for the simulation of seismic waves. In our test examples, the velocities and stresses are zero initially, and a point source is vertically excited near the free surface. The source function is taken as the first derivative of a Gaussian function defined as

$$w(t) = 2\pi f_0(t - t_0)e^{-\pi^2 f_0^2 (t-t_0)^2}$$

where f_0 is the frequency(Hz) and t_0 is a shift in time(s). More precisely, in the equation 4, we set $f_1 = 0$ and f_2 to be a point source with the time component being the first derivative of $w(t)$. In all the examples shown below, the frequency f_0 is 50 Hz and t_0 is 24ms.

We will perform computations in both rectangular and irregular domains. For rectangular domains, we first subdivide the domain into equal size squares, and then we divide each square into two triangles, which forms the initial mesh $\mathcal{T}_h'$. Then we choose the centroid as ν in each triangle and subdivide each triangle into three in the way presented in the previous section. The resulting triangulation is $\mathcal{T}_h$. For computational domains with surface topography, we will use an unstructured mesh as the initial mesh $\mathcal{T}_h'$ near the free surface and use a structured mesh, similar to the one used for rectangular computational domains, as the initial mesh $\mathcal{T}_h'$ for the rest of the computational domain, see Figure 4 for an illustration. The purpose of doing this is to make the simulations more efficient. We remark that the diameter of the triangles in the unstructured mesh is about the same size as the diameters of the triangles in the regular mesh. In all the simulations, we will use $\Delta t \approx 2hC^{-1}$ which is sufficient for stability, where the constant C is determined by equation 44.

For our numerical tests presented below, we will consider the use of four different materials. Their P-wave velocity v_p, S-wave velocity v_s, density ρ, Poisson's ratio ν are summarized in Table 1.

We can then find a time step Δt to ensure the stability by using the method described in the previous section. For example, we obtain $C \approx 8900$ and $C \approx 9130$ for Material 1 and Material 2 respectively. Thus the stability condition for these two cases are $\Delta t < 2.25 \times 10^{-4} h$ and $\Delta t < 2.20 \times 10^{-4} h$ respectively. We remark that this implies that the CFL number, defined as $v_p \Delta t / h$ is approximately 0.117. We recall that the CFL number for the second order finite difference method is about 0.707. Hence the stability condition for our SDG method with piecewise linear elements is approximately 6 times more restrictive than that of the second order finite difference method.

Notice that this fact is partly due to the regularity of the triangles.

In our first example, called example 1, we will perform the simulations of seismic waves for a point source located near a flat surface without the use of PMLs. The domain of interest is $[40\text{m}, 240\text{m}] \times [0\text{m}, 100\text{m}]$ and the physical parameters appearing in the seismic wave equations 3 and 4 are taken as the values for Material 1 defined in Table **??**. We will consider a relatively small simulation time so that no reflection is created from the boundary of the domain, and therefore zero boundary condition for the velocity is assumed. We choose a point source which is vertically excited at [140m, 0m]. For the numerical computations using our SDG method, we take the mesh size $h = 0.167\text{m}$ and the time step size $\Delta t = 0.033\text{ms}$, so that the method is stable and accurate enough. In Figure 5, we present a snapshot of the vertical velocity u_2 at the time $t = 0.25\text{s}$. From this figure, we can see the P- and S-waves as well as the Rayleigh wave. In addition, the faster P-wave, which is travelling at a speed of 520ms^{-1}, has propagated for a distance of about 130m. Also, the slower S-wave, which is travelling at a speed of 300ms^{-1}, has been propagated for a distance of about 75m. On the other hand, we see that the Rayleigh wave is travelling along the free surface and its speed is slightly smaller than that of the S-wave. To show the accuracy of the SDG method, we compare the solution obtained by the SDG method and a reference solution obtained by a fourth order staggered-grid finite difference method on a very fine mesh. In Figure 6, we present this comparison at four different observation points $(160\text{m}, 5\text{m})$, $(180\text{m}, 5\text{m})$, $(200\text{m}, 5\text{m})$ and $(220\text{m}, 5\text{m})$, where the blue curve represents the SDG solution and the red dash line represents the reference solution. From these comparisons, we see clearly that the SDG method gives a very accurate solution. In Figure 7, we present the ability of the SDG method in preserving the wave

energy by computing the relative rate of change of energy over time, which is defined as

$$\delta(t) = \frac{1}{E_\infty}\frac{dE}{dt},$$

where the energy $E(t)$ is given by

$$E(t) = \frac{1}{2}\int_\Omega \left(\rho u_1^2 + \rho u_2^2 + \sigma^T A\sigma\right) dx$$

and E_∞ is the total amount of energy created by the point source. As we can see in Figure 7, the source enters into the computational domain between the initial time and 0.05ms. After this time, we see clearly that the relative rate of change of energy $\delta(t)$ remains zero, confirming the energy conservation property of our scheme. In Figure 8, we present a comparison of seismograms for our SDG solution and the reference solution at the depth $z = 5$m for times up to 0.25s. We again see that our method performs well.

In example 2, we simulate the S-wave and the Rayleigh wave for a material with higher Poisson's ratio. The domain of interest is $[5\text{m}, 45\text{m}] \times [0\text{m}, 15\text{m}]$. The physical parameters appearing in the seismic wave equations 3 and 4 are taken as the values for Material 2 defined in Table **??**. We also apply the multi-axial PMLs (see for example Meza-Fajardo and Papageorgiou (2008)) with 5m width on the boundary of the domain except the free surface. A point source is vertically excited at [10m, 0m]. For the numerical computations by our SDG method, the mesh size $h = 0.05$m and the time step size $\Delta t = 0.01$ms. Snapshots for u_2 at times 0.2s, 0.4s and 0.6s are shown in Figure 9, where the black lines represent the interface between the computational domain and the MPML layers. First of all, we see that the fast P-wave, with a velocity of 520ms^{-1}, has already left the computational domain. With the MPML, the P-wave leaves the domain without much artificial reflection. Moreover, we can see clearly the slower S-wave and the Rayleigh wave near the surface.

The S-wave reaches the lower boundary of the domain and is absorbed by the MPML. In addition, we show the comparison of our solution to the reference solution obtained by a fourth-order finite difference scheme on a very fine mesh at some observation points in Figure 10. It is evident that our SDG method is able to produce accurate numerical solutions, and preserve the wave energy well. We remark that the SDG solution travels a little bit slower than the reference solution, which is due to numerical dispersion. We will discuss more about numerical dispersion at the end of this section.

In our third example, called example 3, we will simulate Rayleigh waves in a heterogeneous material with vertical variations in velocity structure on scales smaller than a wavelength. The domain of interest is $[20\text{m}, 260\text{m}] \times [0\text{m}, 120\text{m}]$. Moreover, the density is 1500 kgm^{-3} and the P-wave and S-wave velocities are described in Figure 11. For the numerical computations, we will apply zero boundary conditions at $x = 0\text{m}$ and $x = 280\text{m}$. The mesh size is taken as 0.2m and the time step size is taken according to the stability condition presented in the previous section. A point source is vertically excited at [140m, 0m] and the snapshot of the solution u_2 at the simulation time $T = 0.4\text{s}$ is shown in Figure 12. From this figure, we see clearly the dispersive behavior of the Rayleigh wave for a vertically varying velocity model is accurately captured. In addition, a comparison of seismograms of the SDG solution and a reference solution is shown in Figure 13. Despite some small differences, we can see that the two solutions have a very good match.

In examples 4 and 5, we demonstrate the ability of our scheme to simulate Rayleigh waves in a domain with surface topography. We assume again that the physical parameters appearing in the seismic wave equations 3 and 4 are taken as the values for Material 2 defined in Table **??**. In example 4, the surface topography is mathematically modelled by the function $\Gamma_4(x) = -4\exp(-\frac{(x-8)^2}{20})$ and

is a convex shaped surface. The computational domain and the MPML are depicted in Figure 13. The point source is vertically excited at [8m, -4m], which is at the top part of the convex region of the free surface. For the numerical computations by our SDG method, the mesh size $h = 0.05$m and the time step size is $\Delta t = 3.33\mu$s to ensure stability and accuracy. We also apply the multi-axial PML with 5m width to absorb outgoing waves. The snapshots of u_2 at times $t = 0.1$s, $t = 0.3$s and $t = 0.5$s are shown in Figure 14. First, we see clearly that the fast P-wave has already left the domain and that the MPML successfully absorbs the outgoing P-wave. On the other hand, the slower S-wave and the Rayleigh wave near the free surface are accurately simulated. We also see that the S-wave is successfully absorbed by the MPML in the left and the lower layers.

In example 5, the surface topography is modelled by the function $\Gamma_5(x) = 3\exp(-\frac{(x-20)^2}{20})$ and is a concave shaped surface. The computational domain and the MPML are depicted in Figure 15. The point source is vertically excited at [6m,0m], which is on the part of the flat surface located on the left of the concave free surface. For the numerical computations by our SDG method, the mesh size $h = 0.05$m and the time step size is $\Delta t = 0.006$ms, and MPML is also used to absorb outgoing waves. The snapshots of u_2 at times $t = 0.1$s, $t = 0.3$s and $t = 0.5$s are shown in Figure 15. We observe similar behaviour as example 4.

In example 6, we consider both surface topography and internal discontinuities. The surface topology is given by $\Gamma_6(x) = -4\exp(-\frac{(x-8)^2}{20})$, which is the same as Γ_4 in example 4. The internal interface between the two layers of different materials is given by $\Gamma_6(x) + 8$. This definition can be seen in Figure 16, where the dotted lines represent the interface between the two materials. The upper layer consists of Material 3 and the lower layer consists of Material 4 in the Table **??** respectively. For the computations by the SDG method, the mesh size is $h = 0.10$m and the time

step size is 0.0125ms so that the method is both stable and accurate. The snapshots of the solution u_2 at times $t = 0.05$s, $t = 0.2$s, $t = 0.3$s and $t = 0.4$s are shown in Figure 16. First, we see the S-wave and the Rayleigh wave are well captured. Moreover, the reflection and transmission of the waves at the internal discontinuities are accurately computed.

Numerical study of dispersion error

In this section, we present a study of the numerical dispersion of our SDG method. The study is based on the eigenvalue method used in Cohen (2002) and Chung et al. (2013a) for the acoustic and electromagnetic wave equations. Let $\mathbf{f} = 0$ in equation 3. We consider a plane wave solution $e^{-i(\mathbf{k}\cdot\mathbf{x}-\omega t)}$ of equations 3 and 4, where $\mathbf{k} = (k_x, k_z)$ is the wave number and ω is the angular frequency. Notice that we have the following well-known dispersion relation:

$$\omega_1 = \frac{1}{\rho}(\lambda + 2\mu)(k_x^2 + k_z^2) \quad \text{and} \quad \omega_2 = \frac{1}{\rho}\mu(k_x^2 + k_z^2). \tag{45}$$

We now consider a rectangular mesh and the SDG system defined in equations 30, 31 and 32 using the piecewise linear approximation. Recall that each rectangle is divided into two triangles, which are denoted generically by $\mathcal{S}(\nu)$. For a given rectangle, we observe that there are totally 24 unknowns in the variable $\vec{\mathbf{u}}$ restricted to this rectangle, and we use $\mathbf{U}$ to represent the vector containing these 24 unknowns. We take the time derivative in equation 30 and use equations 31 and 32 to eliminate the unknown $\vec{\boldsymbol{\sigma}}$, we obtain the following

$$\mathbf{A}_1\mathbf{U}_{tt} = \mathbf{A}_2\widetilde{\mathbf{U}}, \tag{46}$$

where $\mathbf{A}_1$ is a block diagonal mass matrix and $\widetilde{\mathbf{U}}$ is a vector containing all relevant nodal values of $\vec{\mathbf{u}}$. To find the numerical dispersion relation, we substitute the following plane wave solutions in

(46):

$$u_1 = \alpha_r e^{-i(\mathbf{k}\cdot\mathbf{x}-\omega_h t)} \quad \text{and} \quad u_2 = \beta_r e^{-i(\mathbf{k}\cdot\mathbf{x}-\omega_h t)} \tag{47}$$

where α_r and β_r only depends on the relative position of the nodal points, and ω_h is the numerical wave number. Then we obtain the following generalized eigenvalue problem:

$$\omega_h^2 \widetilde{\mathbf{A}}_1 \eta = \widetilde{\mathbf{A}}_2 \eta. \tag{48}$$

Let Λ be the set of all generalized eigenvalues for this problem. Then the dispersion error for ω_1 and ω_2 can be computed by

$$\min_{\omega\in\Lambda} \left| \frac{\omega_1^2}{\omega^2} - 1 \right| \quad \text{and} \quad \min_{\omega\in\Lambda} \left| \frac{\omega_2^2}{\omega^2} - 1 \right|. \tag{49}$$

In Figure 17, we present the results of the SDG numerical dispersion errors using the physical parameters for Material 2 defined in Table **??** and compare them to those obtained from the second and the fourth finite difference methods. In equation 47, we take $\mathbf{k} = (\sqrt{\frac{1}{3}}, \sqrt{\frac{2}{3}})$.

From Figure 17, we see that the dispersion error for our piecewise linear SDG method is smaller than that of the second order finite difference method. Being a second order method, our SDG method performs better in terms of dispersion than second order finite difference method. In addition, we see that the convergence rate of dispersion error for ω_2 is 2 for both our SDG method and the second order finite difference method. Furthermore, for ω_1, we see that the dispersion error has a convergence order of 4, which is the same convergence order for the fourth order finite difference scheme. We also see that the dispersion error for ω_1 for our SDG method is comparable to that of the fourth order finite difference scheme.

Mortar formulation

In this section, we present a strategy specifically designed for the simulation of Rayleigh waves. It is well known that the Rayleigh wave travels along the free surface and decays exponentially in the vertical direction. To make our scheme tailored to this situation, we present a mortar formulation for our SDG method. We assume that the computational domain is divided into two parts, one of them is a thin layer near the free surface. We also assume that a very fine mesh is used for this thin layer and a coarse mesh is used in the rest of the domain. We do not assume that the meshes are matching near the interface $\mathcal{I}$ of these two parts of the computational domain. A schematic in Figure 18 shows this non-matching triangulation.

Let U_h^U and U_h^L be the space for the velocity on the upper mesh and lower mesh respectively. We assume that these two spaces are totally decoupled. We also introduce the space of Lagrange multipliers

$$\widehat{U}_h = U_h^U|_{\mathcal{I}} \tag{50}$$

We will need to modify our SDG method defined in equations 17, 19 and 20 in the following way. We note that equations 19 and 20 can be solved locally in each of the two parts of the computational domain. For equation 17, we need to decouple the velocity unknowns in the two parts of the computational domain and then enforce continuity using the above space of Lagrange multipliers. The resulting scheme reads: find $\mathbf{u}_h \in (U_h)^2$, $\mathbf{\Sigma}_h \in (W_h)^2$, $\mathbf{\Gamma}_h \in X_h$ such that

$$\int_\Omega \rho \frac{\partial \mathbf{u}_h}{\partial t} \cdot \mathbf{v}\, dx + \int_{\mathcal{I}} \hat{\mathbf{u}}_h \cdot \mathbf{v}\, ds + \sum_{\kappa \in \mathcal{F}_u} \Big(\int_{\mathcal{R}(\kappa)} \mathbf{\Sigma}_h \cdot \nabla \mathbf{v}\, dx - \int_{\partial \mathcal{R}(\kappa)} (\mathbf{\Sigma}_h\, \mathbf{n}) \cdot \mathbf{v}\, ds \Big)$$
$$= \int_\Omega \mathbf{f} \cdot \mathbf{v}\, dx, \quad \forall \mathbf{v} \in (U_h)^2, \hat{\mathbf{v}} \in (\widehat{U}_h)^2.$$

$$\int_{\mathcal{I}} [\mathbf{u}_h] \cdot \hat{\mathbf{v}}\, ds = 0 \quad \forall \hat{\mathbf{v}} \in (\hat{U}_h)^2.$$

$$\int_\Omega \mathbf{A} \frac{\partial \mathbf{\Sigma}_h}{\partial t} \cdot \boldsymbol{\alpha}\, dx + \sum_{\nu \in \mathcal{N}} \Big(\int_{\mathcal{S}(\nu)} \mathbf{u}_h \operatorname{div} \boldsymbol{\alpha}\, dx - \int_{\partial \mathcal{S}(\nu)} \mathbf{u}_h \cdot (\boldsymbol{\alpha}\, \mathbf{n})\, ds \Big) + \int_\Omega \mathbf{\Gamma}_h \cdot \boldsymbol{\alpha}\, dx = 0, \quad \forall \boldsymbol{\alpha} \in (W_h)^2.$$

$$\int_\Omega \boldsymbol{\Sigma}_h \cdot \boldsymbol{\eta}\, dx = 0, \quad \forall \boldsymbol{\eta} \in X_h$$

where $[\hat{\mathbf{u}}_h]$ is the jump of $\mathbf{u}_h$ across the mesh interface $\mathcal{I}$. We apply this method to the same Material in example 1 with same domain of interest and source position. The interface of the two meshes is located at $z = 6$m. The mesh size for the upper mesh is 0.167m and the mesh size for the lower mesh is 0.5m. The time step size $\Delta t = 0.033$ms. In Figure 19, we present the snapshot of the solution u_2 at the time $t = 0.25$s and in Figure 20, we present a comparison of the numerical solution and the reference solution at various observation points from the initial time up to time equals 0.25s. To compare this example with example 1, we compute the relative error defined by $\frac{\|u_2 - u_{2,ref}\|_2}{\|u_{2,ref}\|_2}$ at $z = 5$m and $0 \leq t \leq 0.25$s, where $u_{2,ref}$ is the reference solution for u_2. The relative error for example 1 and the mortar example is 0.18% and 0.22% respectively. The results show that the mortar formulation produces equally accurate results. Moreover, in the current setting in which the coarse mesh size is three times larger than the fine mesh size, the speed up is about 5.2 times.

CONCLUSIONS

We developed an SDG method for the velocity-stress formulation of elastic waves. Moreover, by using a mortar formulation, our method can be used for the simulations of Rayleigh waves. The method enjoys several distinctive features that are particularly attractive: first, it conserves the wave energy automatically; second, it is optimally convergent in both L^2-norm and energy norm; third, only solutions of a block diagonal linear system and a local saddle point system are needed in each time step, giving a very efficient time marching scheme; fourth, it is flexible in handling complex geometries so that free surface conditions on nonflat surfaces can be imposed easily; fifth,

it yields solutions with extremely low dispersion errors. Numerical examples have shown that the SDG method provides a competitive alternative for simulations of seismic and Rayleigh waves with irregular surface topography.

ACKNOWLEDGEMENTS

The research of Eric Chung is partially supported by Hong Kong RGC General Research Fund (Project: 400813) and CUHK Direct Grant for Research (2013/14). The research of Jianliang Qian is partially supported by NSF.

REFERENCES

Ainsworth, M., P. Monk, and W. Muniz, 2006, Dispersive and dissipative properties of discontinuous Galerkin finite element methods for the second-order wave equation: Journal of Scientific Computing, **27**, 5–40.

Aki, K., and P. G. Richards, 2002, Quantitative seismology: University Science Books.

Appelö, D., and N. A. Petersson, 2009, A stable finite difference method for the elastic wave equation on complex geometries with free surfaces: Communications in Computational Physics, **5**, 84–107.

Arnold, D. N., 1982, An interior penalty finite element method with discontinuous elements: SIAM Journal on Numerical Analysis, **19**, 742–760.

Basabe, J. D., and M. K. Sen, 2009, New developments in the finite-element method for seismic modeling: The Leading Edge, **28**, 562–567.

Becache, E., P. Joly, and C. Tsogka, 2000, An analysis of new mixed finite elements for the approximation of wave propagation problems: SIAM J. Numer. Analy., **37**, 1053–1084.

Bernacki, M., S. Lanteri, and S. Piperno, 2006, Time-domain parallel simulation of heterogeneous wave propagation on unstructured grids using explicit, nondiffusive, discontinuous Galerkin methods: Journal of Computational Acoustics, **14**, 57–81.

Bohlen, T., and E. H. Saenger, 2006, Accuracy of heterogeneous staggered-grid finite-difference modeling of Rayleigh waves.: Geophysics, **71**, 109–115.

Bourdel, F., P.-A. Mazet, and P. Helluy, 1991, Resolution of the non-stationary or harmonic Maxwell equations by a discontinuous finite element method: Application to an E.M.I. (electromagnetic impulse) case: Proceedings of the 10th international conference on computing methods

in applied sciences and engineering, Nova Science Publishers, Inc., 405–422.

Chan, H., E. Chung, and G. Cohen, 2013, Stability and dispersion analysis of staggered discontinuous Galerkin method for wave propagation.: Int. J. Numer. Anal. Model., **10**, 233–256.

Chung, E., and P. Ciarlet, 2013, A staggered discontinuous Galerkin method for wave propagation in media with dielectrics and meta-materials.: J. Comput. Appl. Math., **239**, 189–207.

Chung, E., P. Ciarlet, and T.F.Yu, 2013a, Convergence and superconvergence of staggered discontinuous Galerkin methods for the three-dimensional maxwell's equations on cartesian grids.: J. Comput. Phys., **235**, 14–31.

Chung, E., B. Cockburn, and G. Fu, 2014a, The staggered DG method is the limit of a hybridizable DG method.: SIAM J. Numer. Anal., **52**, 915–932.

Chung, E., and B. Engquist, 2006, Optimal discontinuous Galerkin methods for wave propagation.: SIAM J. Numer. Anal., **44**, 2131–2158.

———, 2009, Optimal discontinuous Galerkin methods for the acoustic wave equation in higher dimensions.: SIAM J. Numer. Anal., **47**, 3820–3848.

Chung, E., and H. Kim, 2014, A deluxe FETI-DP algorithm for a hybrid staggered discontinuous Galerkin method for H(curl)-elliptic problems.: Internat. J. Numer. Methods Engrg, **98**, 1–23.

Chung, E., H. Kim, and O. Widlund, 2013b, Two-level overlapping schwarz algorithms for a staggered discontinuous Galerkin method.: SIAM J. Numer. Anal., **51**, 47–67.

Chung, E., and C. Lee, 2012, A staggered discontinuous Galerkin method for the curl-curl operator.: IMA J. Numer. Anal., **32**, 1241–1265.

Chung, E., M. Yuen, and L. Zhong, 2014b, A-posteriori error analysis for a staggered discontinuous Galerkin discretization of the time-harmonic Maxwell's equations.: Appl. Math, Comput., **237**,

613–631.

Cockburn, B., G. E. Karniadakis, and C.-W. Shu, 2000, Discontinuous Galerkin methods: Theory, computation and applications: Springer.

Cohen, G., 2002, Higher-order numerical methods for transient wave equations: Springer.

Cohen, G., P. Joly, N. Tordjman, and J. Roberts, 2001, Higher order triangular finite elements with mass lumping for the wave equation: SIAM J. Numer. Analy., **38**, 2047–2078.

De Basabe, J. D., M. K. Sen, and M. F. Wheeler, 2008, The interior penalty discontinuous Galerkin method for elastic wave propagation: grid dispersion: Geophysical Journal International, **175**, 83–93.

Dumbser, M., and M. Kaser, 2006, An arbitrary high-order discontinuous Galerkin method for elastic waves on unstructured meshes-II. The three-dimensional isotropic case: Geophys. J. Internat., **167**, 319–336.

Falk, R. S., and G. R. Richter, 1999, Explicit finite element methods for symmetric hyperbolic equations: SIAM Journal on Numerical Analysis, **36**, 935–952.

Geveci, T., 1988, On the application of mixed finite element methods to the wave equation: RAIRO Model. Math. Anal. Numer., **22**, 243–250.

Giraldo, F. X., J. S. Hesthaven, and T. Warburton, 2002, Nodal high-order discontinuous Galerkin methods for the spherical shallow water equations: Journal of Computational Physics, **181**, 499–525.

Graves, R. W., 1996, Simulating seismic wave propagation in 3d elastic media using staggered-grid finite differences: Bulletin of the Seismological Society of America, **86**, 1091–1106.

Grote, M. J., A. Schneebeli, and D. Schötzau, 2006, Discontinuous Galerkin finite element method

for the wave equation: SIAM Journal on Numerical Analysis, **44**, 2408–2431.

Hestholm, S., and B. Ruud, 2002, 3d free-boundary conditions for coordinate-transform finite-difference seismic modelling: Geophysical Prospecting, **50**, 463–474.

Hu, F. Q., M. Y. Hussaini, and P. Rasetarinera, 1999, An analysis of the discontinuous Galerkin method for wave propagation problems: Journal of Computational Physics, **151**, 921–946.

Johnson, C., and J. Pitkäranta, 1986, An analysis of the discontinuous Galerkin method for a scalar hyperbolic equation: Math. Comp., **46**, 1–26.

Kim, H., E. Chung, and C. Lee, 2013, A staggered discontinuous Galerkin method for the Stokes system.: SIAM J. Numer. Anal., **51**, 3327–3350.

———, 2014, A BDDC algorithm for a class of staggered discontinuous Galerkin methods.: Comput. Math. Appl., **67**, 1373–1389.

Komatitsch, D., F. Coutel, and P. Mora, 1996, Tensorial formulation of the wave equation for modelling curved interfaces: Geophysical Journal International, **127**, 156–168.

Komatitsch, D., J. Labarta, and D. Michea, 2008, A simulation of seismic wave propagation at high resolution in the inner core of the Earth on 2166 processors of MareNostrum: Lecture Notes in Computer Science, **5336**, 364–377.

Komatitsch, D., and J. P. Vilotte, 1998, The spectral-element method: an efficient tool to simulate the seismic response of 2D and 3D geological structures: Bull. Seis. Soc. Am., **88**, 368–392.

Kosloff, D., and J. M. Carcione, 2010, Two-dimensional simulation of Rayleigh waves with staggered sine/cosine transforms and variable grid spacing.: Geophysics, **75**, 133–140.

Lesaint, P., and P. A. Raviart, 1974, On a finite element method for solving the neutron transport equation (Proc. Symposium, Mathematical Research Center): Mathematical aspects of finite

elements in partial differential equations, Academic Press, 89–123.

Levander, A. R., 1988, Fourth-order finite-difference p-sv seismograms: Geophysics, **53**, 1425–1436.

Lombard, B., J. Piraux, C. Gélis, and J. Virieux, 2008, Free and smooth boundaries in 2-d finite-difference schemes for transient elastic waves: Geophysical Journal International, **172**, 252–261.

Ma, S., R. J. Archuleta, and P. Liu, 2004, Hybrid modeling of elastic p-sv wave motion: a combined finite-element and staggered-grid finite-difference approach: Bulletin of the Seismological Society of America, **94**, 1557–1563.

Madariaga, R., 1976, Dynamics of an expanding circular fault: Bull. Seis. Soc. Am., **66**, 639–666.

Meza-Fajardo, K., and A. Papageorgiou, 2008, A nonconvolutional, split-field, perfectly matched layer for wave propagation in isotropic and anisotropic elastic media: stability analysis: Bulletin of the Seismological Society of America, **98**, 1811–1836.

Moczo, P., E. Bystrickỳ, J. Kristek, J. M. Carcione, and M. Bouchon, 1997, Hybrid modeling of p-sv seismic motion at inhomogeneous viscoelastic topographic structures: Bulletin of the Seismological Society of America, **87**, 1305–1323.

Patera, A. T., 1984, A spectral element method for fluid dynamics: Laminar flow in a channel expansion: J. Comput. Phys., **54**, 468–488.

Raviart, P. A., and J. M. Thomas, 1977, A mixed finite element method for 2nd order problems: Presented at the Mathematical Aspects of the Finite Element Method, Lecture Notes in Math. 606, Springer-Verlag, Berlin, Heidelberg, New York.

Reed, W. H., and T. R. Hill, 1973, Triangular mesh methods for the neutron transport equation: Technical Report LA-UR-73-479, Los Alamos Scientific Laboratory, Los Alamos, USA.

Rivière, B., and M. F. Wheeler, 2003, Discontinuous finite element methods for acoustic and elastic

wave problems: Contemporary Mathematics, **329**, 271–282.

Riviere, B. M., 2008, Discontinuous Galerkin methods for solving elliptic and parabolic equations: Theory and implementation: SIAM.

Robertsson, J. O., 1996, A numerical free-surface condition for elastic/viscoelastic finite-difference modeling in the presence of topography: Geophysics, **61**, 1921–1934.

Seriani, G., and E. Priolo, 1994, Spectral element method for acoustic wave simulation in heterogeneous media: Finite Element in Analysis and Design, **16**, 337–348.

Stenberg, R., 1988, A family of mixed finite elements for the elasticity problem: Numer. Math., **53**, 513–538.

Virieux, J., 1986, P-SV wave propagation in heterogeneous media: Velocity-stress finite-difference method: Geophysics, **51**, 889–901.

Zahradnik, J., P. Moczo, and F. Hron, 1993, Testing four elastic finite-difference schemes for behavior at discontinuities: Bulletin of the Seismological Society of America, **83**, 107–129.

Zeng, C., J. Xia, R. D. Miller, and G. P. Tsoflias, 2012, An improved vacuum formulation for 2D finite-difference modeling of Rayleigh waves including surface topography and internal discontinuities.: Geophysics, **77**, 1–9.

Zhang, W., and X. Chen, 2006, Traction image method for irregular free surface boundaries in finite difference seismic wave simulation: Geophysical Journal International, **167**, 337–353.

LIST OF FIGURES

14 Snapshots for the vertical velocity u_2 in example 4. The black lines indicate the interface between the domain of interest and the MPMLs.

15 Snapshots for the vertical velocity u_2 in example 5. The black lines indicate the interface between the domain of interest and the MPMLs.

16 Snapshots for the vertical velocity u_2 in example 6. The black lines indicate the interface between the domain of interest and the MPMLs. The dotted lines indicate the interface between the two materials.

17 The comparison of dispersion error for our SDG method and finite difference schemes.

18 A non-matching mesh used for the mortar formulation of our SDG method.

19 The snapshot for the vertical velocity u_2 at t = 0.25s for the mortar formulation applying to the same model in example 1.

20 Comparsion of the mortar solution (SDG) to a reference solution at the same observation points as in example 1.

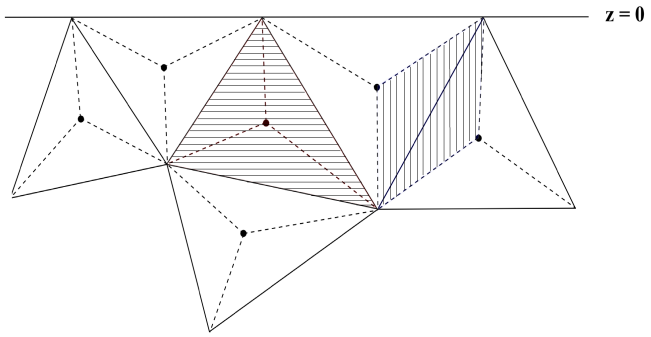

Figure 1: An example of the initial triangulation $\mathcal{T}_h'$ (denoted by solid lines) and the subdivision of triangles of $\mathcal{T}_h'$ by interior points (denoted by solid dots). The newly formed edge in the subdivision process is denoted by dotted lines. The shaded region with horizontal lines is an example of a macro element $\mathcal{S}(\nu)$ while the shaded region with vertical lines is a macro element $\mathcal{R}(\kappa)$.

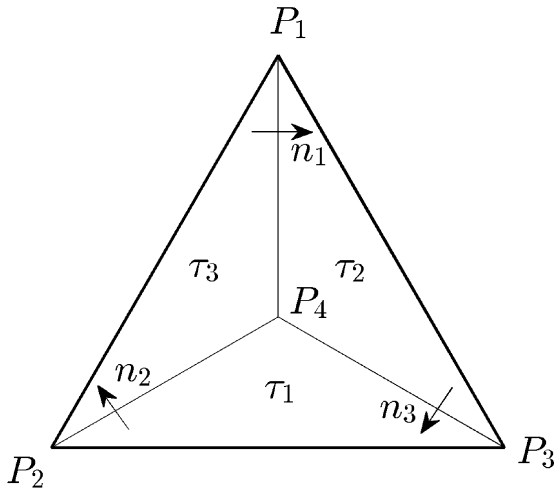

Figure 2: Notations for the construction of basis for W_h.**Chung et al.** –

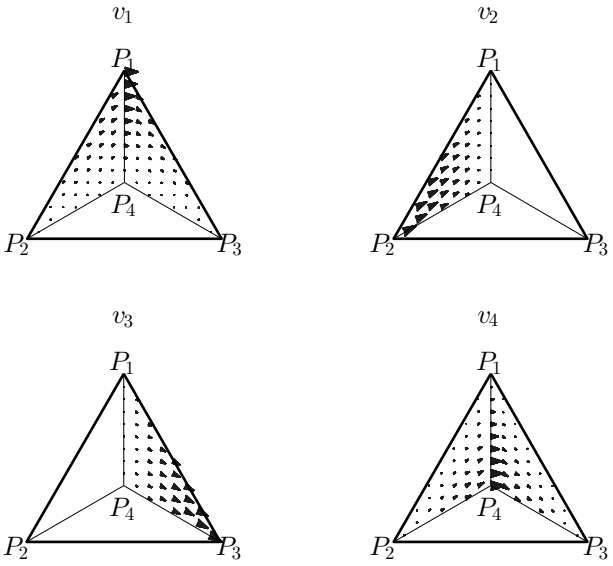

Figure 3: Plots of the first-type basis functions for W_h on $S(\nu)$ with $m = 1$.**Chung et al.** –

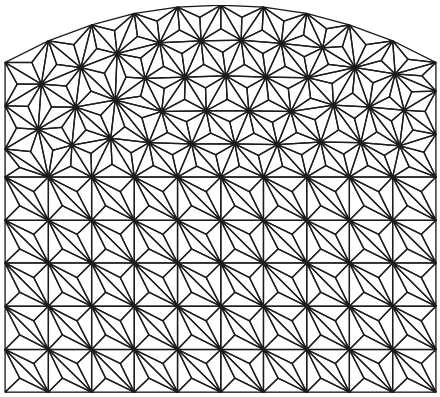

Figure 4: A schematic for an initial triangulation for computational domains with surface topography, where unstructured mesh is used near free surface and regular mesh is used for the rest of the domain.

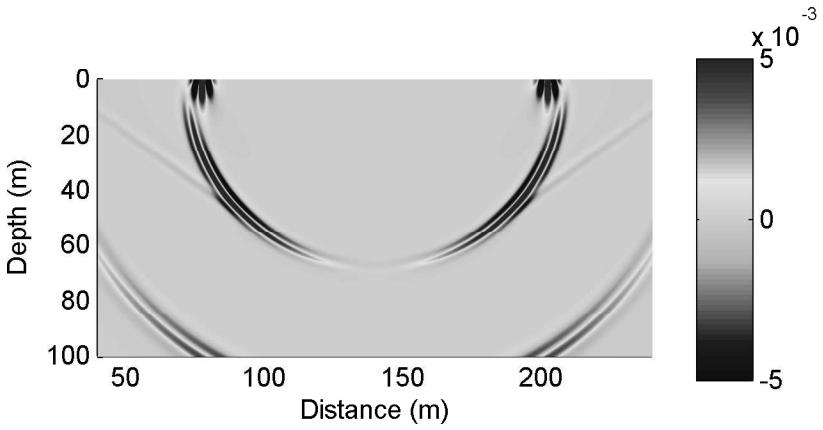

Figure 5: The snapshot for the vertical velocity u_2 at $t = 0.25s$ in example 1. **Chung et al.** –

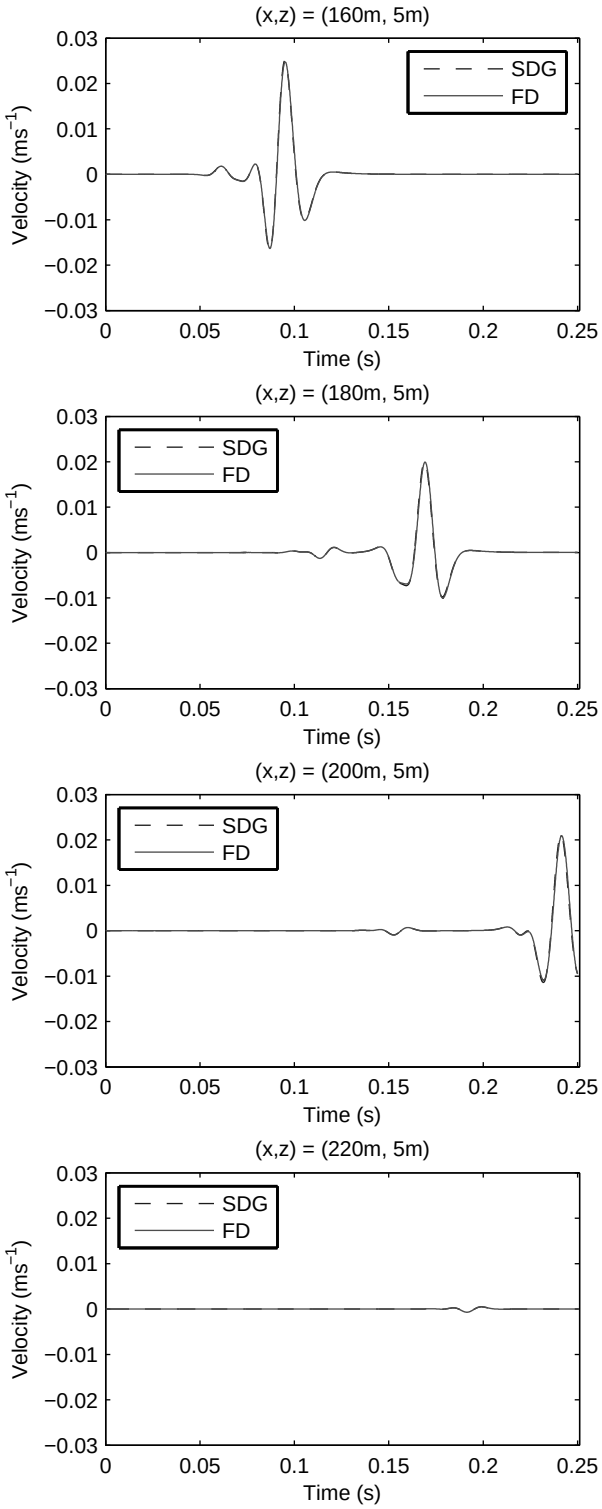

Figure 6: Comparison of our solution (SDG) to a reference solution at various observation points in example 1.

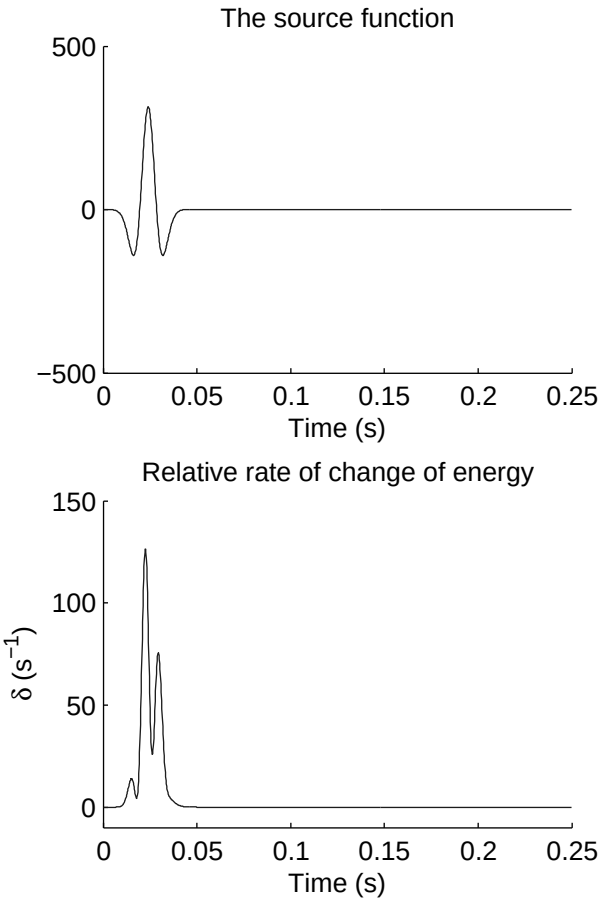

Figure 7: The source function and the relative rate of change of the energy over time in example 1.

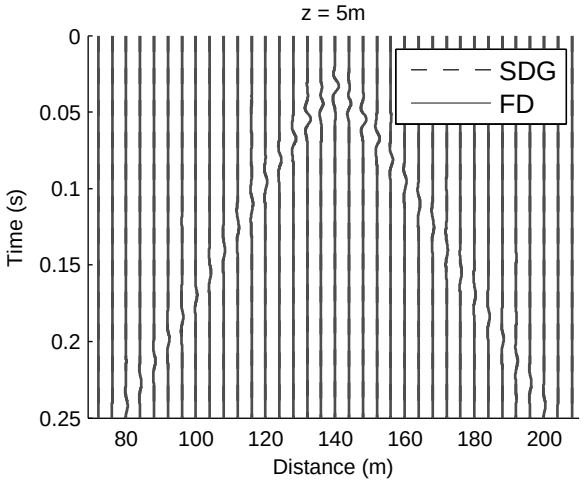

Figure 8: Comparison of seismograms with the SDG and the reference solutions for example 1.

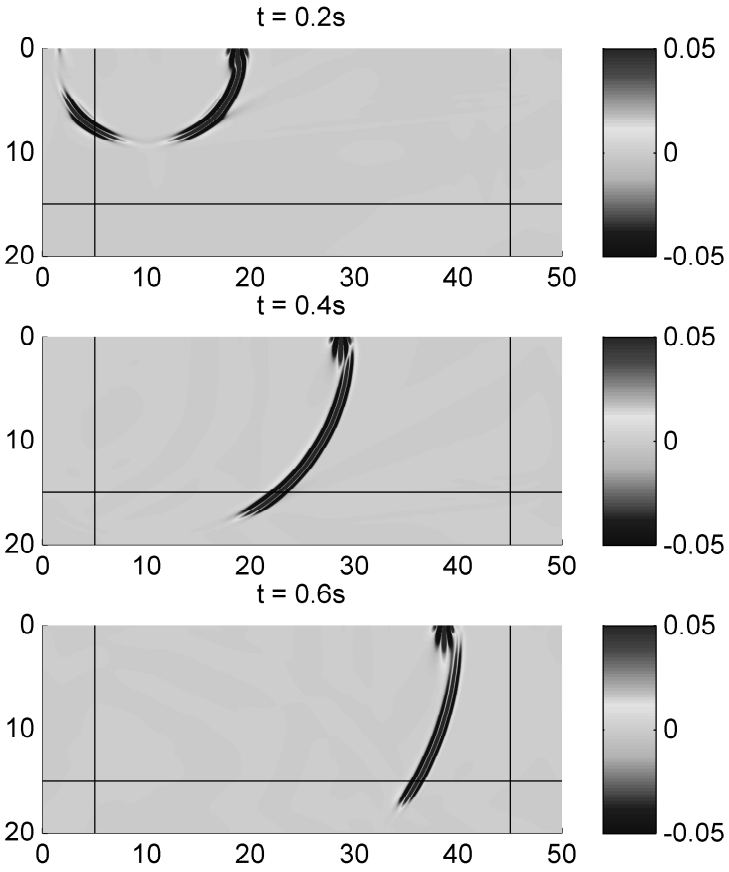

Figure 9: Snapshots for the vertical velocity u_2 in example 2. The black lines indicate the interface between the domain of interest and the MPMLs.

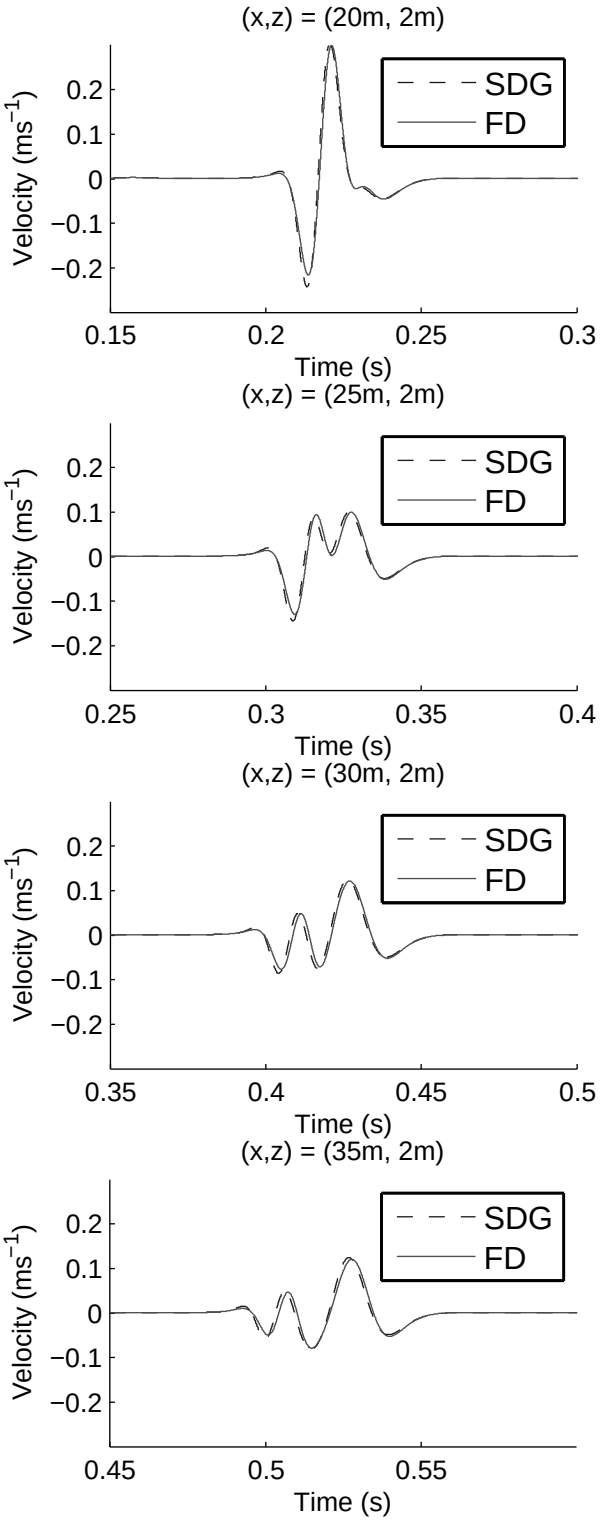

Figure 10: Comparison of our solution (SDG) to a reference solution at various observation points in example 2.

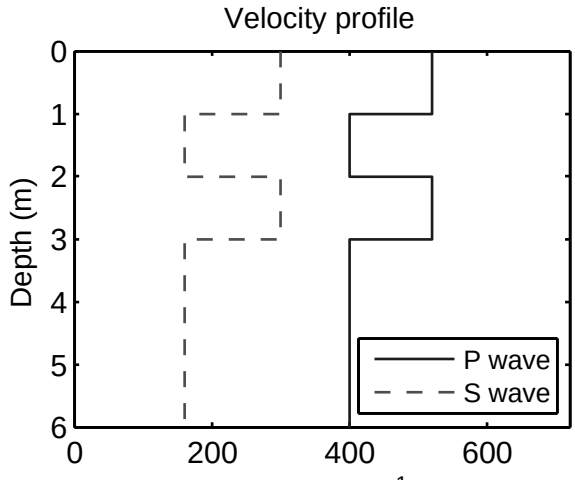

Figure 11: The velocity profiles along the depth for example 3.**Chung et al.** –

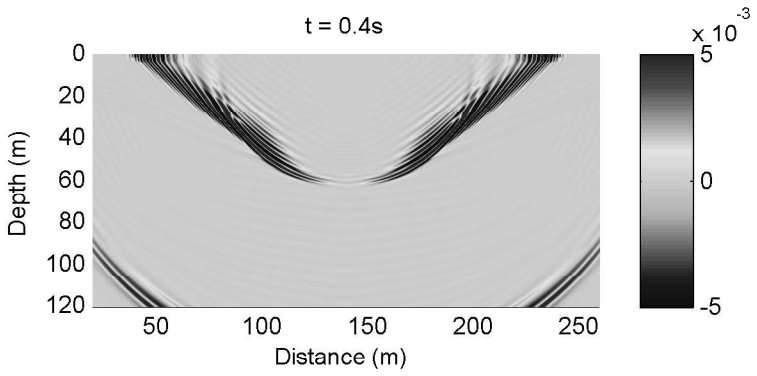

Figure 12: The snapshot for vertical velocity u_2 at $T = 0.4$s in example 3.**Chung et al.** –

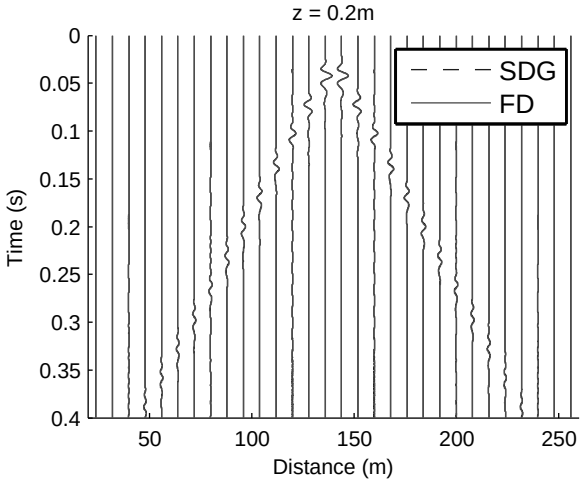

Figure 13: A comparison of seismograms of the SDG solution and a reference solution for example 3.

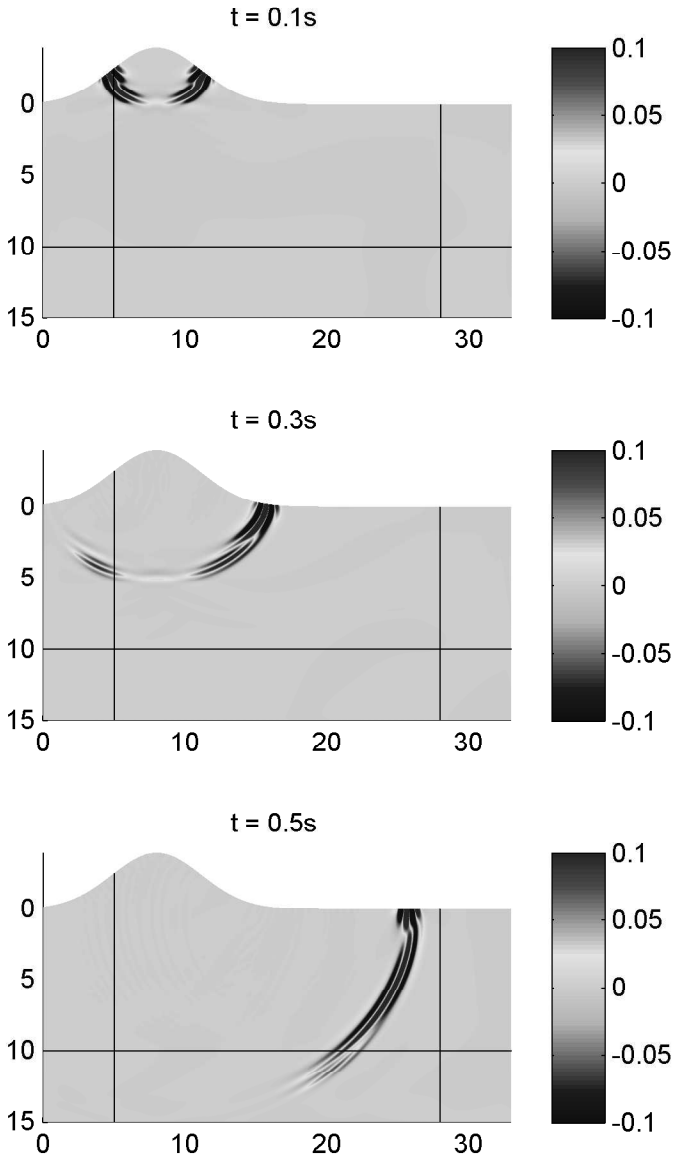

Figure 14: Snapshots for the vertical velocity u_2 in example 4. The black lines indicate the interface between the domain of interest and the MPMLs.

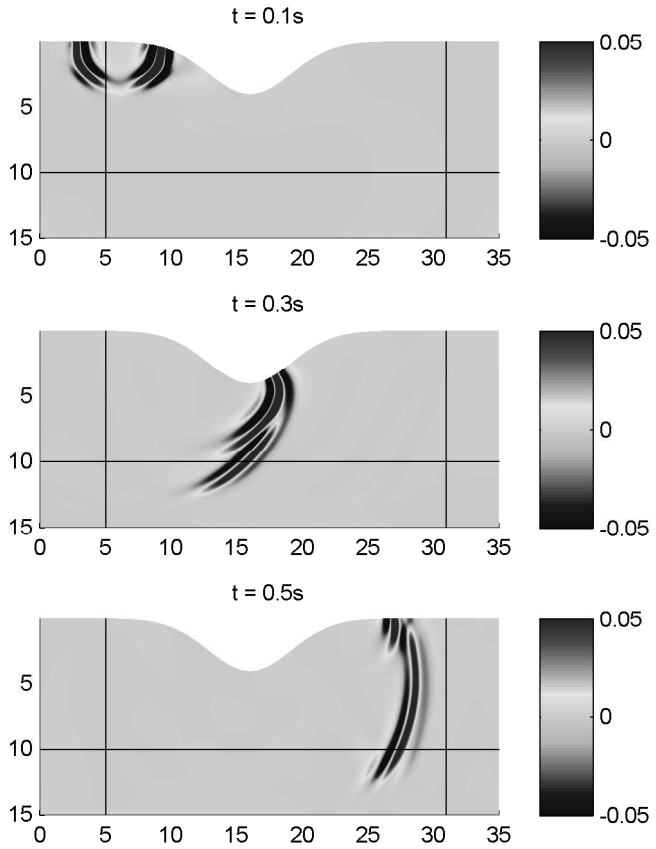

Figure 15: Snapshots for the vertical velocity u_2 in example 5. The black lines indicate the interface between the domain of interest and the MPMLs.

Chung et al. –

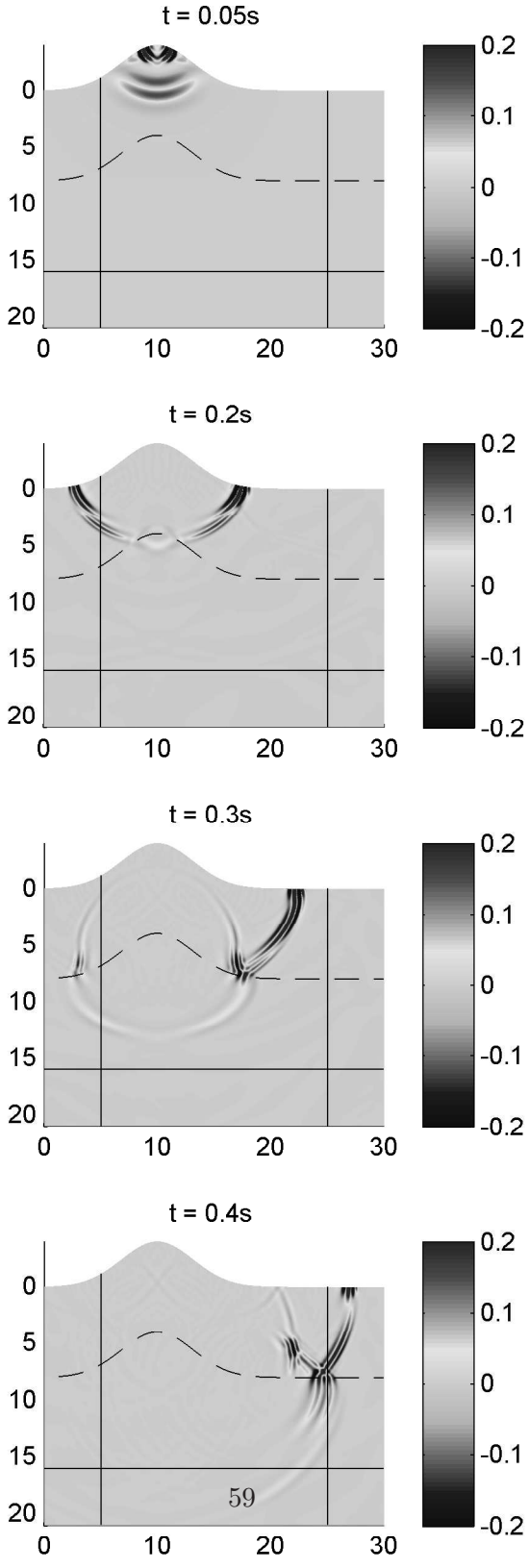

Figure 16: Snapshots for the vertical velocity w_2 in example 6. The black lines indicate the interface

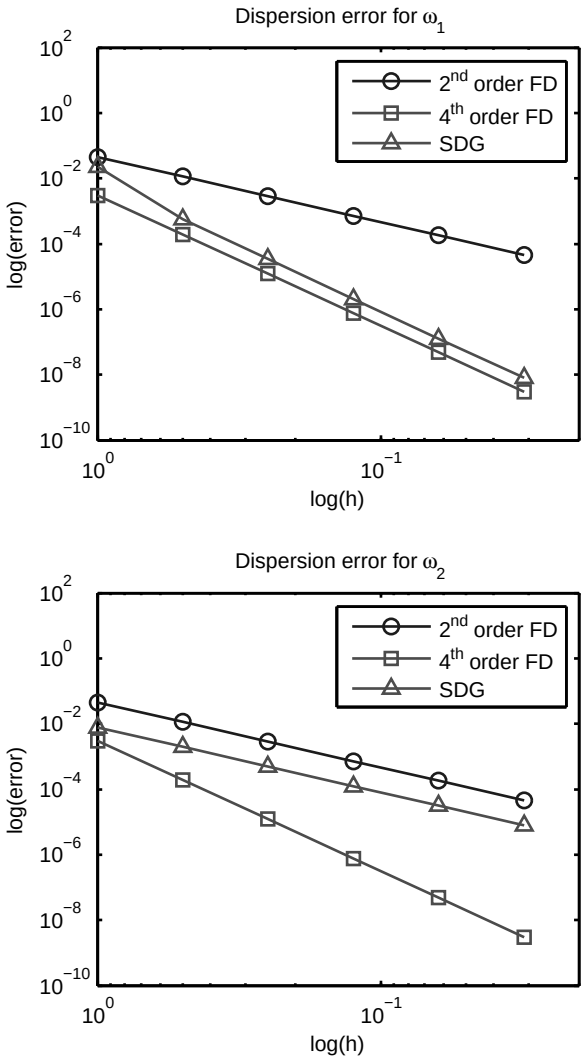

Figure 17: The comparison of dispersion error for our SDG method and finite difference schemes.

Chung et al. –

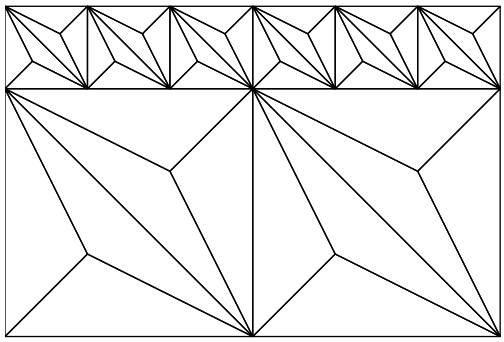

Figure 18: A non-matching mesh used for the mortar formulation of our SDG method.

Chung et al. –

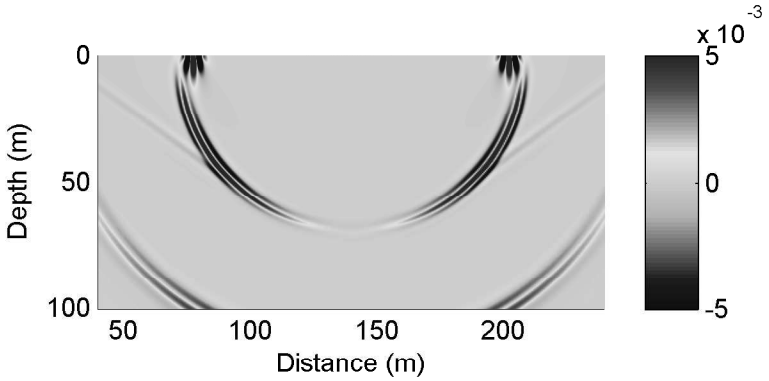

Figure 19: The snapshot for the vertical velocity u_2 at t = 0.25s for the mortar formulation applying to the same model in example 1.

Chung et al. –

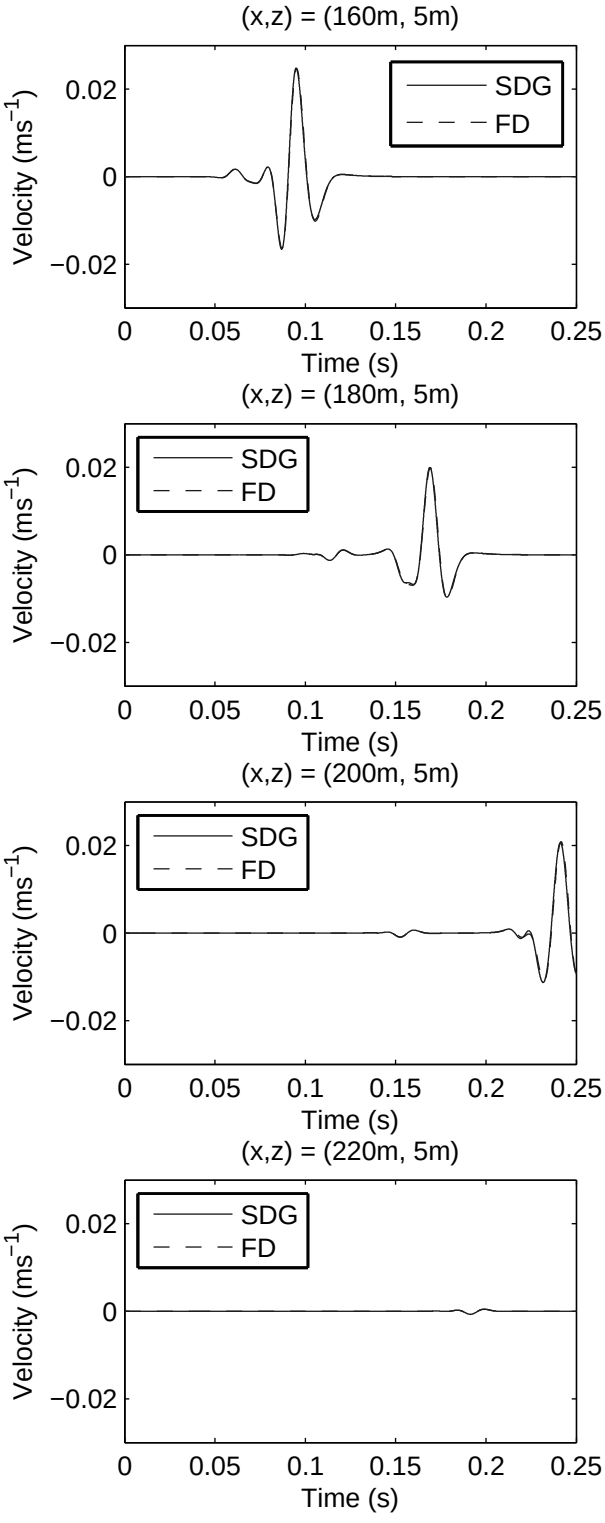

Figure 20: Comparsion of the mortar solution (SDG) to a reference solution at the same observation points as in example 1.